Sulfur tolerant sub-nano Fe/alumina catalysts for propane dehydrogenation

Lohit Sharma,¹ Stephen C. Purdy,² Katharine Page,^{2,3,4} Srinivas Rangarajan¹ Hien Pham,⁵ Abhaya Datye⁵ and Jonas Baltrusaitis^{1,*}

- Department of Chemical and Biomolecular Engineering, Lehigh University, 111
 Research Drive, Bethlehem, PA 18015, USA
- Neutron Scattering Division, Oak Ridge National Laboratory, Oak Ridge, TN 37830, USA
- 3. Shull Wollan Center, Oak Ridge National Laboratory, Oak Ridge, TN 37830, USA
- 4. Materials Science and Engineering Department, University of Tennessee, Knoxville, TN 37996, USA
 - 5. Center for Microengineered Materials and Department of Chemical & Biological Engineering, University of New Mexico, Albuquerque, NM 87131, USA.

Abstract

A series of Al₂O₃-supported Fe-containing catalysts were synthesized by incipient wetness impregnation. The iron surface density was varied from 1 to 13 Fe atoms/nm² spanning sub- and above-monolayer coverage. The resulting supported Fe-catalysts were characterized with N₂ physisorption, *ex situ* XRD, PDF, XAS, AC-STEM and chemically probed by H₂-TPR. The results suggest that over this entire range of loadings, Fe was present as dispersed species, with only a very small fraction of Fe₂O₃ aggregates, at the highest Fe loading. The *in situ* sulfidation of Fe/Al₂O₃ resulted in the formation of a highly active and selective PDH catalyst. The highest activity with 52% propane conversion and ~99% propylene selectivity at 560 °C was obtained for the 6.4 Fe/Al₂O₃ catalyst suggesting that this is the highest amount of Fe that could be fully dispersed on the support in sulfided form. XRD and AC-STEM indicated the absence of any crystalline iron sulfide aggregates after sulfidation and reaction. H₂-TPR results indicated that the amount of the reducible Fe sites in the sulfided catalyst remained constant above monolayer coverage, and increasing loading did not increase the number of reducible Fe sites. Consistent with these results, the reactivity per gram of catalyst showed no increase with Fe loading above monolayer coverage, suggesting that additional Fe remains conformal to the alumina surface.

Corresponding author: Jonas Baltrusaitis: job314@lehigh.edu

1.0 Introduction

The demand for alkenes, such as propylene, has increased by a 4% compounded annual growth rate during the last decade. It is further expected to increase in the upcoming years. ^{1–3} The non-oxidative dehydrogenation of propane (PDH) can selectively produce propylene from abundant natural gas resources. ⁴ During the PDH, activation of propane C–H bonds governs the overall catalytic performance. However, propylene, once formed, is more reactive than propane. This leads to further side reactions including cracking, deep dehydrogenation, and polymerization, typically resulting in low process selectivity and catalyst deactivation. Significant research efforts have focused on Cr and Pt-alloys to achieve and sustain the activity of the catalysts as well as their selectivity and stability. ⁵ However, the high cost of Pt, its propensity to sinter at high temperatures, and its susceptibility to poisoning in the presence of sulfur compounds have led to research into catalyst material alternatives. In particular, there has been a growing interest in earth-abundant and environmentally benign catalytic materials, such as oxides of Fe, Cu, Co, Ga, Zn, V, Mo, Zr, and Sn, for selective dehydrogenation of propane. ^{6–15} However, these metal oxide-based catalysts (i) are not sufficiently active, (ii) suffer from low selectivity, (iii) and coke formation caused rapid deactivation, and (iv) their stability needs to be further improved. ^{5,16}

An alternative to improve the activity and selectivity is the addition of sulfur species over some PDH catalysts. For example, Resasco *et al.*¹⁷ determined that when Ni/Al₂O₃ was treated with dimethyl sulfoxide, it exhibited improved selectivity and decreased coke formation during the isobutane (i-C₄) dehydrogenation. Wang *et al.*^{18,19} have studied supported metals of Co, Cu, Mo, Mn, Zn, Fe on SiO₂ and determined that these H₂/H₂S pretreated catalysts exhibited higher propane selectivity. For example, the selectivity of about 87% was observed compared to 43% in the case of 13 Fe/SiO₂, and activity was five times higher than the corresponding oxide phase during i-C₄ dehydrogenation. A more recent work by Cheng and coworkers has investigated bulk and supported MoS₂ and showed that the rate of i-C₄ dehydrogenation over the supported catalyst was ~7 times higher than the bulk catalyst.²⁰ Recently, several studies examined the propensity and stability of a Fe-based catalyst for non-oxidative and oxidative PDH. For example, Fe-based catalysts (such as Fe/ZSM-5) were used for oxidative propane dehydrogenation.^{21,22} Fe-based catalysts were also studied for non-oxidative propane dehydrogenation.^{6,23,24} Lobo *et al.*²⁵ demonstrated that isolated Fe in a zeolite framework (Fe-ZSM-5) is an efficient PDH catalyst. A

series of works by Li and coworkers^{26,27} investigated the non-oxidative PDH over 20% Fe/SO₄²⁻/Al₂O₃. It was proposed that the addition of the sulfur species as SO₄²⁻ was responsible for improved catalytic performance due to the electron-withdrawing effect of SO₄²⁻ species from metal ions.

Recently, Watanabe *et al.*^{28,29} investigated SiO₂ supported Fe, Ni, and Co for PDH in the presence of H₂S. Their study showed that 20 Fe/SiO₂ after exposure to H₂S could selectively activate propane. The authors proposed that Fe_(1-x)S was the active phase for the reaction based on XRD, XPS, XAS techniques. These experiments were performed using the catalyst with a high fixed Fe metal loading of 20 wt.% supported on SiO₂. At this Fe loading, the active catalytic phase can consist of Fe as monomers, oligomers as well as crystalline FeS_x. It is generally accepted that at high loadings, Fe can result in 3d Fe₂O₃-like aggregates.³⁰ In contrast, Fe at low loadings leads to highly dispersed iron oxide clusters.^{24,31,32} For example, it was determined that the catalytic activity during SCR is closely related to the number of Fe sites, particularly dispersed and oligomeric clusters,^{31,32} whereas aggregated moieties reveal relatively low activity.³³ It is possible that at high loading, both dispersed and aggregated Fe structures are present. Presently, all the state-of-the-art work is performed at fixed Fe loading for the chemistry.^{6,23–29} The catalytic behavior of dispersed and aggregated Fe species on supports for PDH has yet to be determined, especially in the presence of H₂S.

In this context, we have performed a systematic study of Fe loading over Al₂O₃ with incipient wetness impregnation. As shown in **Figure 1**, we find that the Fe species remain atomically dispersed, essentially in sub-nano form, over the entire range of Fe loadings we studied.

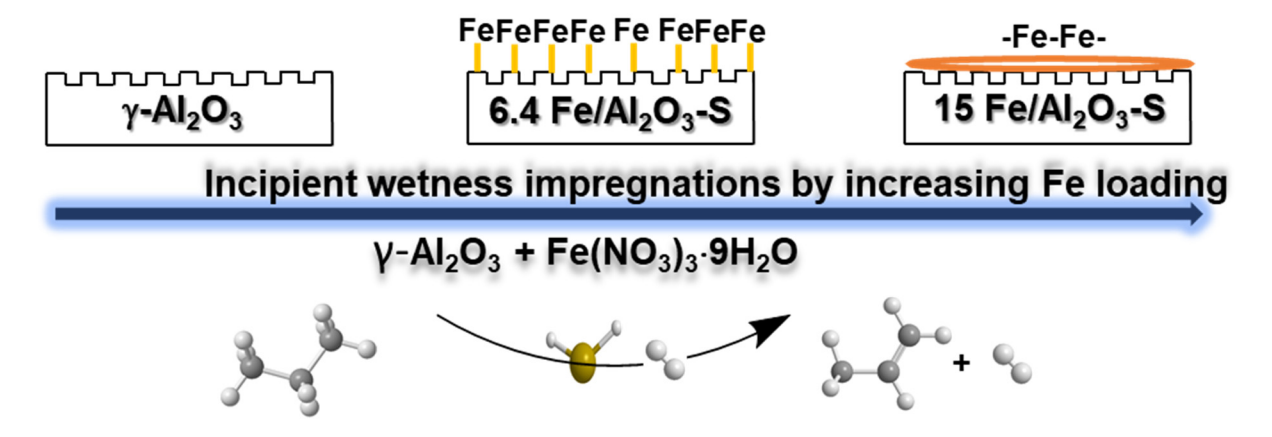


Figure 1. Schematic diagram showing the nature of the Fe sub-nano species in catalysts prepared via incipient wetness impregnation. After sulfiding, these dispersed Fe sites are active and selective for propane dehydrogenation, in the presence of H₂S.

We explored the potential of Fe/Al₂O₃ as an earth-abundant and relatively inexpensive catalyst for propane activation in the presence of H₂S. In this study, we have synthesized catalysts with a known weight loading of Fe metal and determined their local atomic coordination to develop insights regarding the structure and the oxidation states. Further, the number of reducible iron species was determined using H₂-TPR. Here, we report that Fe/Al₂O₃ is very selective for propane dehydrogenation (>99% at 52% conversion at T=560 °C and C₃H₈:H₂:H₂S: N₂=1.1:1:0.1:97.8) upon pretreatment with and co-feed of H₂S (esp. 0.1 mol% co-feed), underlining the high activity-selectivity potential of the catalyst. This systematic study of Fe-based catalysts shows the vital role of dispersed Fe sites for the PDH chemistry. It will help design improved catalysts for PDH from a molecular perspective.

2.0 Experimental Methods

Materials and reagents.

γ-Al₂O₃ (Sasol, Catalox SBA-150) was received from Sasol. 10 % H₂, 10 % C₃H₈, and 1 % H₂S (all diluted with N₂) were purchased from Airgas. Fe(NO₃)₃·9H₂O and FeS were purchased from Acros Organics. Fe₃O₄ and Fe₂O₃ were purchased from Aldrich.

Catalyst synthesis and activation with H₂S for propane dehydrogenation reaction

The γ -Al₂O₃ was calcined at 600 °C for 4 h under flowing air before impregnation. Fe(NO₃)₃·9H₂O was dissolved in 0.5 M HNO₃ solution in DI water. The Fe/Al₂O₃ catalysts were prepared by incipient wetness impregnation of an aqueous solution of Fe(NO₃)₃·9H₂O onto calcined γ -Al₂O₃ support. The impregnation step was performed under ambient conditions, and the impregnated mixture was stirred for ~30 min to maximize FeO_x dispersion. The catalyst was then dried overnight in ambient conditions. Later, the catalyst was dried with flowing air (1 L/min) at 120°C for 4 hours and calcined at 600°C for 4 hours under flowing air and a 1.33 °C/min ramp rate using a programmable furnace. The final synthesized catalysts are denoted as x Fe/Al₂O₃, where x is the weight percent of Fe impregnated on the support. Before the reaction, as synthesized x Fe/Al₂O₃

oxide catalysts were exposed to the stream of H_2S ($P_{H_2S} = 0.01$ atm, the balance N_2) at 600 °C for 4 hours. The calcined catalysts are referred to as x Fe/Al₂O₃ (e.g., 10 Fe/Al₂O₃ or 10 Fe), whereas H_2S pretreated catalysts are referred to as x Fe/Al₂O₃-S (e.g., 10 Fe/Al₂O₃-S or 10 Fe (S)). Finally, if catalysts were characterized after one PDH cycle, they are referred to as x Fe/Al₂O₃-S1 (e.g., 10 Fe/Al₂O₃-S1 or 10 Fe (S1)).

 N_2 -Physisorption studies. The surface areas of the catalysts were measured via nitrogen physisorption (-196 °C) using a Micromeritics ASAP 2020 instrument.³⁴

Transmission Electron Microscopy (TEM)

The air-exposed, powder samples were dispersed in ethanol and supported on holey carbon films on Cu grids for TEM. A JEOL NeoARM 200 CF microscope, operated at 200 kV, was used for this study. The spherical aberration corrector in this microscope provides a resolution of 0.71 Å. A JEOL dual EDS system using Oxford AZTEC software was used for elemental analysis via x-ray fluorescence in the TEM. Images using a 30 µm condenser aperture and 8 cm detector camera length in annular dark field (ADF) mode images were recorded simultaneously with annular bright field (ABF) images.

X-ray Diffraction (XRD).

The powder XRD and x-ray pair distribution function (PDF) measurements were performed at the PDF beamline (ID-28-1) of the National Synchrotron Light Source II. Samples were loaded into 1 mm OD Kapton tubes and sealed at both ends with epoxy. Measurements were made using an X-ray wavelength of 0.16635 Å and a Perkin Elmer large area detector. The sample to detector distance for XRD and PDF measurements was 240 cm and 840 cm, respectively. For both distances, a CeO₂ standard was used for detector calibration.

Detector calibration, 2D pattern masking, and 2D pattern integration were performed using DIOPTAS software.³⁵ The reduced pair distribution function, G(r), was extracted from I(q) data using the program PDFgetx3.³⁶ A q range of 0.9 to 23.0 Å⁻¹ was used for all samples for the Fourier transform, and the R_{poly} value was set to 0.9. Background subtraction was done using a scan of an empty Kapton capillary. Small box modeling of the PDF was done using PDFgui software.³⁷

X-ray Absorption Spectroscopy. X-ray Absorption Spectroscopy at the iron K edge (7110.7 eV) was performed at the MRCAT bending magnet line (10-BM) of the Advanced Photon Source, Argonne National Laboratory.³⁸ Catalysts for XAS were ground into a fine powder and pressed into a self-supporting pellet. Catalysts were mounted in a Nylon washer and secured with Kapton

tape. Measurements were performed in fluorescence mode using a vortex 4 element detector. The monochromator energy was calibrated using the inflection point of iron foil, with the absolute energy taken from literature.³⁹ Scans were taken in step scanning mode over an energy range of 6910 eV to 7657 eV, giving a k-max of 11.8 Å⁻¹. Each catalyst was scanned 3 times and averaged to give the analyzed spectra.

Data reduction and analysis were performed using the Demeter software suite. The edge energy was taken as the first derivative maximum of the rising edge of the XANES. The pre-edge energy was taken as the point of maximum intensity (first derivative zero) of the pre-edge peak. The absolute energy resolution of the monochromator (Si 111) at the Fe K-edge is 0.8 eV (1x10⁻⁴ ΔΕ/Ε), and the sample-to-sample variation in energy was better than 0.1 eV. Self-absorption artifacts were removed using the FLUO algorithm implemented in Athena.⁴⁰ The nominal composition of the catalyst and the sample to beam angle (45°) were used as inputs for the correction. Normalization was performed using a first-order polynomial for the pre-edge (-200 to 30 eV) and a third-order polynomial for the post edge (125 eV to 535 eV). Bare atom absorption was subtracted using a spline fit over the entire measured k range and used an R_{bkg} value of 1.0. Fitting was performed in R-space over a k-range of 2.7-11.0 Å⁻¹ and an R range of 1.0-3.0 Å, giving 10 free parameters. All models used fewer free parameters than were available based on Nyquist theorem.

Models were constructed using a bulk crystallographic reference of Fe₂O₃. All paths shared an E₀ correction, and all bond distances were correlated through an isotropic lattice expansion coefficient ε , where the bond distance for each path was defined as:

$$R = R_{eff} * (1 + \varepsilon) \tag{1}.$$

For samples with Fe-Al scattering, the Fe₂O₃ FEFF input file generated by Artemis was modified by replacing neighboring Fe atoms with Al. The first shell oxygen scattering was fit using two separate oxygen paths sharing a single Debye-Waller factor. Similarly, the second shell was fit using two Fe-Al single scattering paths with a single Debye-Waller factor. Each path was given a separate coordination number. Allowing for separate Debye-Waller factors for each oxygen path did not significantly improve fit statistics or change the fit coordination numbers for each path. The amplitude reduction factor S_0^2 for all samples and paths was fixed to the value fit iron foil using a bulk BCC Fe model. Full details of the Fe foil fit are given in the Supplemental Information.

H₂-Temperature Programmed Reduction (H₂-TPR). H₂-TPR was performed using the same steady-state reactor used for kinetic studies equipped with an MKS Cirrus 2 mass spectrometer. A \sim 75 mg of the catalyst was loaded into the reactor and pretreated at 300 °C for 1 hr with a 20 °C /min ramping rate under 30 mL/min 2% O₂/N₂ flow for the as-synthesized catalyst (non H₂S treated). After cooling down to 30 °C in N₂, N₂ was replaced with 2% H₂/N₂ at 25 ml/min for 15 minutes. In the following step, the temperature was ramped to 800 °C at 10 °C/min in 2% H₂/N₂. The sulfided catalyst was prepared by pretreating at 600 °C for 4 hours in 1% H₂S/N₂. Subsequently, the catalyst was flushed in N₂ for 15 minutes. After cooling down to 30 °C in N₂, 2% H₂/N₂ was flown at 30 mL/min for 15 minutes. In the following step, the temperature was ramped to 800 °C at 10 °C/min in 2% H₂/N₂ flow. The calibrated H₂-TPR was utilized to calculate the number (moles) of H₂ consumed. For calibration, at least four different CuO amounts were utilized to determine the number of H₂ atoms consumed. ⁴¹ The standard error was estimated to be about 4% based on the calibration curve obtained using CuO, Fe₂O₃ and Fe₃O₄ standards. It was observed that catalyst after H₂S pretreatment resulted in the evolution of H₂S during H₂-TPR (Fe- $S + H_2 \rightarrow Fe + H_2S$). Concurrently, the number of H_2 molecules consumed was calculated and used to determine the number of reducible Fe present on the surface, assuming H₂:Fe was 1:1.

Steady-state catalytic reactivity testing. The steady-state kinetic experiments were performed in a quartz tube reactor (6.8 mm I.D). All reported steady-state experiments were carried out using either 200 mg or 30 mg of catalyst, with the reactor operating at 1 atm with negligible pressure drop. Quartz wool was placed in the reactor to support the catalyst bed. The temperature was ramped at 20 °C/min to 600 °C. Typically, the catalyst was pretreated in a stream of H_2S ($P_{H_2S} = 0.01$ atm, the balance N_2) at 600 °C for 4 hours. The catalyst was labeled as Fe/Al₂O₃-S if the catalyst was pretreated in the H_2S stream. More details regarding the experimental setup can be found in the previous work. The number of reducible [Fe] sites were determined using H_2 -TPR. The rate (based on C_3H_8 conversion per second per g of catalyst) and selectivity were calculated according to equations (3) through (6). The reaction rate represented is multiplied by 10^7 and the conversion is extensively reported in the SI.

$$rate \left(\frac{mol}{g*s}\right) = \frac{conversion*inlet concentration (C_3H_8)*flowrate \left(\frac{ml}{min}\right)*\left(\frac{1}{60}\frac{min}{s}\right)*\left(\frac{1}{1000}\frac{L}{ml}\right)}{\left(22.4\frac{L}{mol}\right)*Loading Weight(g)}$$
(2),

$$Selectivity (\%) = \frac{[C_3H_6]_{out}}{[C_3H_8]_{in} - [C_3H_8]_{out}} * 100$$
(3),

Conversion (%) =
$$\frac{[C_3H_8]_{in} - [C_3H_8]_{out}}{[C_3H_8]_{in}} * 100$$

$$TOF (s^{-1}) = \frac{rate}{Number of reducible sites [Fe]}$$
(5),
$$F/I = \frac{Final \ reaction \ rate \ (TOS=10 \ hr)}{Intial \ rate \ (TOS=5 \ min)}$$
(6).

The carbon balance for the reaction was 100% within experimental error. The reaction temperature of 560 °C was selected for the study. A low concentration of C₃H₈ (1.1 mol%) was used to conduct experiments safely to reduce the flow and concentration of H₂S in the co-feed while maintaining the C₃H₈:H₂S (1:0.1) ratio in the reactant stream.⁴⁴ This is consistent with the literature where propane dehydrogenation reactions are carried out between 450-650°C with C₃H₈ feed concentration varying from 1.5-20 mol%. The first data point was collected after 5 minutes timeon-stream (TOS) under given reaction conditions. Replicate experiments reproduced reaction rates within $\pm 5\%$, and selectivity can be reproduced within $\pm 2\%$. The reaction studies typically were performed using N₂ dilution (1.1% C₃H₈, 97.8% inert (N₂), 1% H₂, and 0.1% H₂S). Therefore, the mole change during the reaction was ignored, and it was assumed that the volumetric flow rate remains constant.⁴⁵ High conversion data were obtained using 200 mg catalyst and a total volumetric flow rate of 50 ml/min. The catalyst amount was reduced to 30 mg to obtain data under differential conditions. The total volumetric flow rate was also increased to 75 ml/min. At the same time, the gas composition was maintained as indicated above by adjusting the flow rate. The catalyst was uniformly mixed with 150 mg sand. The thermal conversion was low (<0.1%). However, at low conversion, the moles of CH₄ and C₂H₄ formed due to gas phase reaction were comparable. The selectivity value has been corrected for background contributions from thermal cracking of propane, as measured over sand under the same conditions. At 560 °C, propane conversion due to cracking amounts to 0.1% and is $\sim 60\%$ selective to propene. At the end of the reaction, the catalyst was purged, cooled to room temperature under N₂, removed from the reactor, and stored in a glass vial for spectral characterization.

3.0 Results

3.1 Catalyst textural property characterization. N₂ sorption has been used to measure the textural properties of the as-synthesized catalysts. The N₂ adsorption-desorption isotherms shown in Figure S1a followed type IV isotherms with distinct hysteresis loops indicating their mesoporosity which are observed when monolayer and multilayer adsorption of N₂ occurs. An Increasing the Fe loading led to a continuous decrease in the BET surface area but the loss of surface area can be explained by a conformal layer of the Fe species which only add weight to the catalyst, but do not increase the physical surface area. The loss of pore volume is likewise consistent with this picture, since the pore sizes based on the Barrett, Joyner, and Halenda (BJH) remained unchanged with Fe loading as shown in Figure S1b. The formation of second feature around 8 nm at the highest weight loading is consistent with the likely presence of a small fraction of Fe₂O₃ aggregates, as we show later. The corresponding surface area, pore volume, pore size, and the Fe loading (atoms-nm⁻²) are summarized in Table 1.

Table 1. Summary of textural properties of various Fe loading (wt.%) over Al₂O₃ after calcination in air at 600°C for 4 hr.

Catalyst	Surface area ^a	Pore volume	Pore size (nm)	Coverage, Fe
	(m^2/g)	(cm^3/g)		atoms·nm ⁻² , ^b
Al ₂ O ₃	142	0.45	15	0
1.5 Fe/Al ₂ O ₃	142	0.45	15	1.14
3 Fe/Al ₂ O ₃	140	0.42	15	2.28
5 Fe/Al ₂ O ₃	138	0.41	8,15	3.91

6.4 Fe/Al ₂ O ₃	134	0.38	8,15	5
10 Fe/Al ₂ O ₃	132	0.37	8,15	8.17
15 Fe/Al ₂ O ₃	120	0.31	8,15	13.26

^aThe surface area is based on the BET method. Pore size is based on the BJH method. ^bFe, atoms⋅nm⁻², were estimated on the assumption that all Fe is fully dispersed over Al₂O₃.

3.2 Powder X-ray diffraction (XRD) and X-ray pair distribution function (PDF)

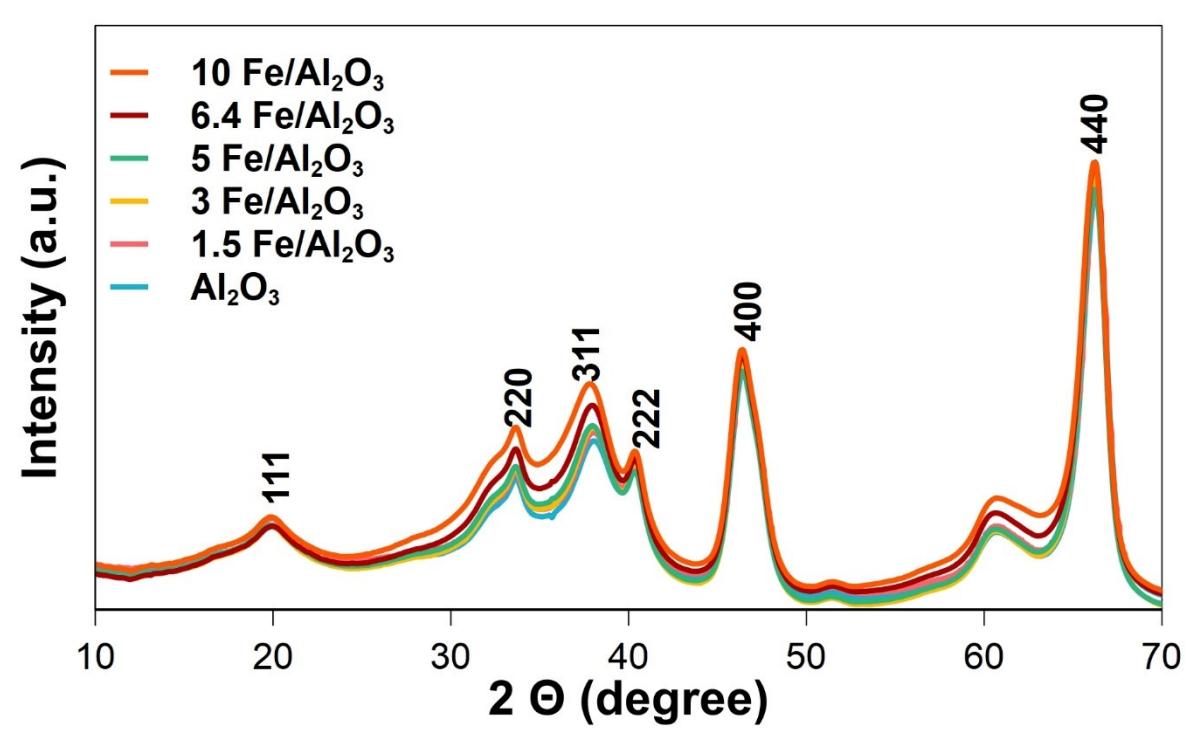


Figure 2. Synchrotron XRD patterns of Fe/Al₂O₃ catalysts. Fe/Al₂O₃ represents as-synthesized catalyst after calcination in air at 600°C for 4 hr.

Synchrotron XRD patterns were used to analyze the phase composition of the as-synthesized catalysts, and the bare γ -Al₂O₃ support is shown in **Figure 2**. Peaks characteristic of γ - Al₂O₃ are seen, and no contribution from other crystalline phases is evident. Diffraction peaks in the patterns associated with the aluminum sublattice: (111), (220), (311), (222) are broadened and asymmetric due to antiphase and rotational boundaries, while the well-ordered oxygen sublattice peaks (400) (440) are sharp and symmetric.⁴⁸ As Fe loading is increased, several of the broad asymmetric peaks

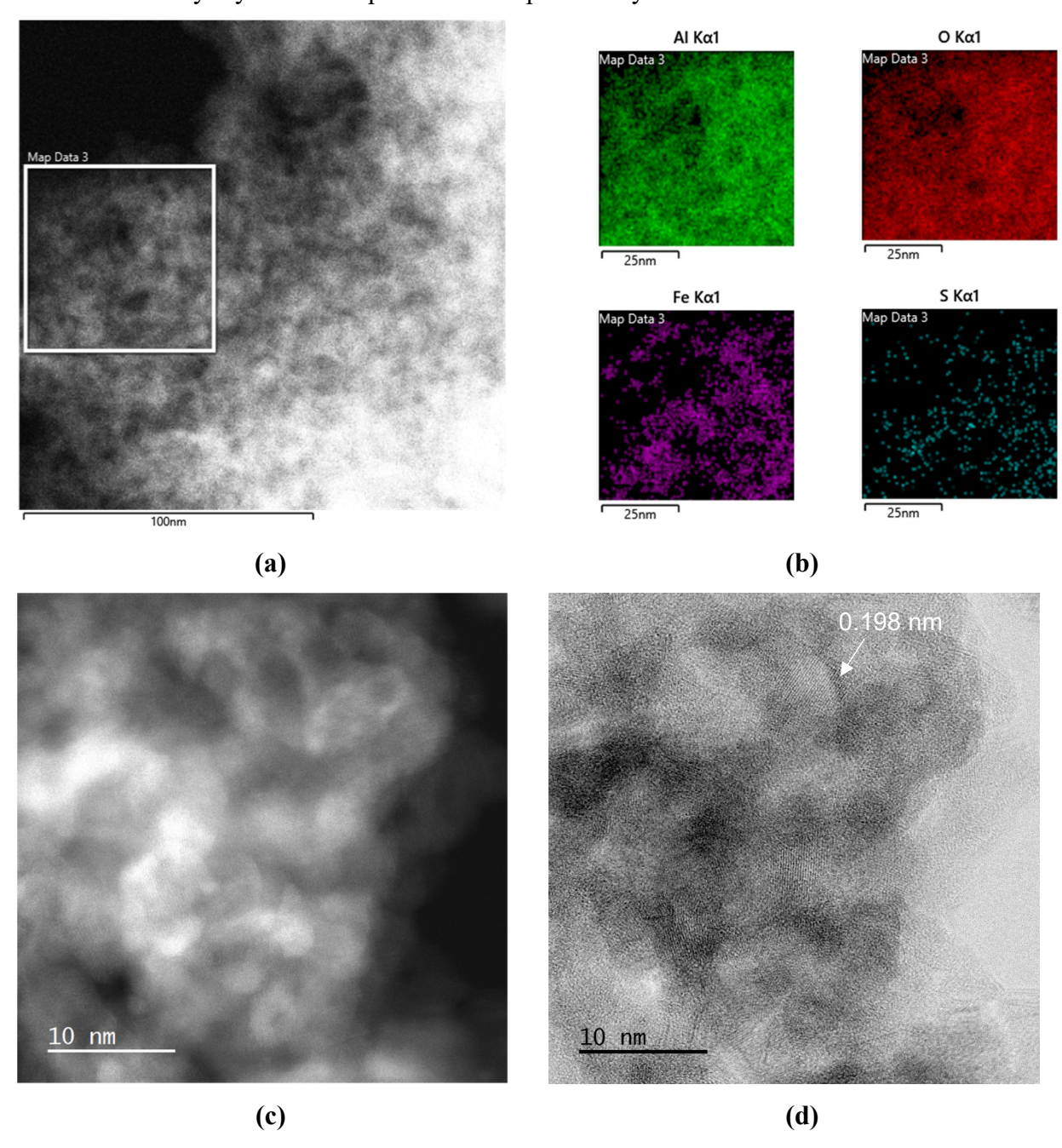
increase in intensity relative to the oxygen lattice peaks. This is attributed to iron adsorption onto different surface planes of alumina, which modifies the structure factor of their respective Bragg peak. Note that despite the increase in structure factor for the aluminum sublattice peaks, there is no peak shift, which suggests that iron is not incorporating into the bulk of Al₂O₃. These results suggest that iron species on alumina are only ordered over a very short range at all loadings. Subsequently, non-synchrotron XRD was also utilized to study as-synthesized and the spent catalyst and the results are discussed in Figure S2. The diffraction peaks related to the Fe₂O₃ crystalline phase were absent even for the highest loading of 15% Fe indicating either an amorphous nature or dispersed state with no long-range order.⁴⁹ TEM results confirm this picture and show that there are no detectable crystalline phases other than alumina (Figures S3, S4 and S5). The STEM ADF images are ideal for detecting the presence of the heavier element (Fe) on the lighter Al₂O₃ support. While higher contrast regions were seen, they did not reveal any lattice fringes corresponding to iron oxides. The only crystalline phase detected was gamma alumina. The EDS map (Figure S6) shows that Fe is well dispersed even in the 15wt% Fe sample. Some regions show higher concentration of Fe. These regions, however, do not yield any lattice fringes corresponding to iron oxides, so we infer that they could amorphous or poorly crystallized Fe oxide. The absence of any visible large particles confirms that the Fe is well dispersed, even on the 15 wt% Fe sample. This sample was also studied in its sulfided form (Figures S7 – S9) showing very similar structure, i.e. Fe is well dispersed while EDS confirms the sample is sulfided.

To gain further insight into the local iron structure, a locally sensitive technique, pair distribution function was measured on the catalysts. The X-ray pair distribution function (PDF) of Fe/Al₂O₃ catalysts, as well as the bare Al₂O₃ support, are plotted in **Figure S10a**. Below 8 Å, the series shows several peaks that have changed in intensity relative to the bare support, whereas as longer length scales, the patterns only show minor variation. This result is in line with the XRD results showing only changes in the relative intensity of a subset of diffraction peaks and the diffuse scattering background. The changes in relative intensity are due to scattering pairs involving iron, which due to having a higher x-ray scattering length, leads to higher intensity peaks. To determine whether the local Fe structure is better represented by substitution of alumina or by a subnanometer sized iron oxide phase, a difference analysis was performed by subtracting the scaled Al₂O₃ pattern from each Fe/Al₂O₃ catalyst.

Figure S10b shows the difference patterns for Fe/Al₂O₃ catalysts. The Fe loading for 1.5 Fe/Al₂O₃ was too low to produce a difference spectra signal above the noise and hence was not included. The residual peaks left after the difference represent the modification of the support due to Fe loading. Qualitatively, this allows the determination of the coherent length scale of iron species on the catalyst. Looking at the first 5 Å, the remaining peaks align well with the local structure of Fe₂O₃, which suggests that iron has not substituted into the Al₂O₃ structure but rather is present as sub-nanometer surface Fe₂O₃ species. Past 5 Å, the Fe₂O₃ and difference patterns do not match, which suggests that the length scale of iron species on the support is on the order of 1-2 coordination polyhedra. Residual signal not associated with the iron structure reflects subtle structural changes of the Al₂O₃ support.

Previously, Xie et al. ⁵⁰ suggested that iron oxides form a monolayer on the γ-Al₂O₃ surface. They reported a Fe loading threshold of 0.052 g Fe₂O₃ per 100 m² Al₂O₃ or ~4 Fe atoms nm⁻² to form monolayer coverage. Similarly, other studies also suggested that iron can be dispersed between 4-5.5 Fe atoms nm⁻² over y-Al₂O₃ support. Accordingly, the XRD and PDF results in this work indicate the possibility of forming a highly dispersed Fe-phase. Notably, temperatures higher than 1000 °C are usually required to form aluminate spinel (FeAlO₃) or crystalline hercynite (FeAl₂O₄) from Fe_2O_3 and Al_2O_3 . 52,53 The XRD pattern of the Fe/Al_2O_3 -S1 catalysts after one complete PDH cycle (Figure S2d) with H2S co-feed were also acquired. Similar to the fresh catalysts, no diffraction peaks for crystalline phases other than γ -Al₂O₃, such as FeS_x,⁵⁴ were observed. The results indicate the lack of any bulk like FeS_x species. Of note, the spent catalyst was exposed to air before the examination, which may result in partial oxidation of the catalyst. The 6.4 Fe catalyst was also studied via AC-STEM after one cycle of PDH. While regions of higher contrast are seen in the EDS map (Figure 3), there is no corresponding crystalline phase detected in the images, the only crystalline structures observed correspond to the alumina as seen in the higher magnification images. Higher magnification images show contrast ascribed to single atoms of Fe, confirming that the Fe remains atomically dispersed in this sample after reaction. These catalysts were also air exposed, but EDS shows evidence for Fe and S (Figures S8 and S9). After recording images from 50 regions of this sample, we found only one that contained a crystalline Fe particle (Figure S11). We include this only to show that if such particles were present, they would be readily

visible in the AC-STEM images, since the microscope resolution is 0.71 Å. These results confirm the absence of any crystalline Fe phases in the spent catalyst.



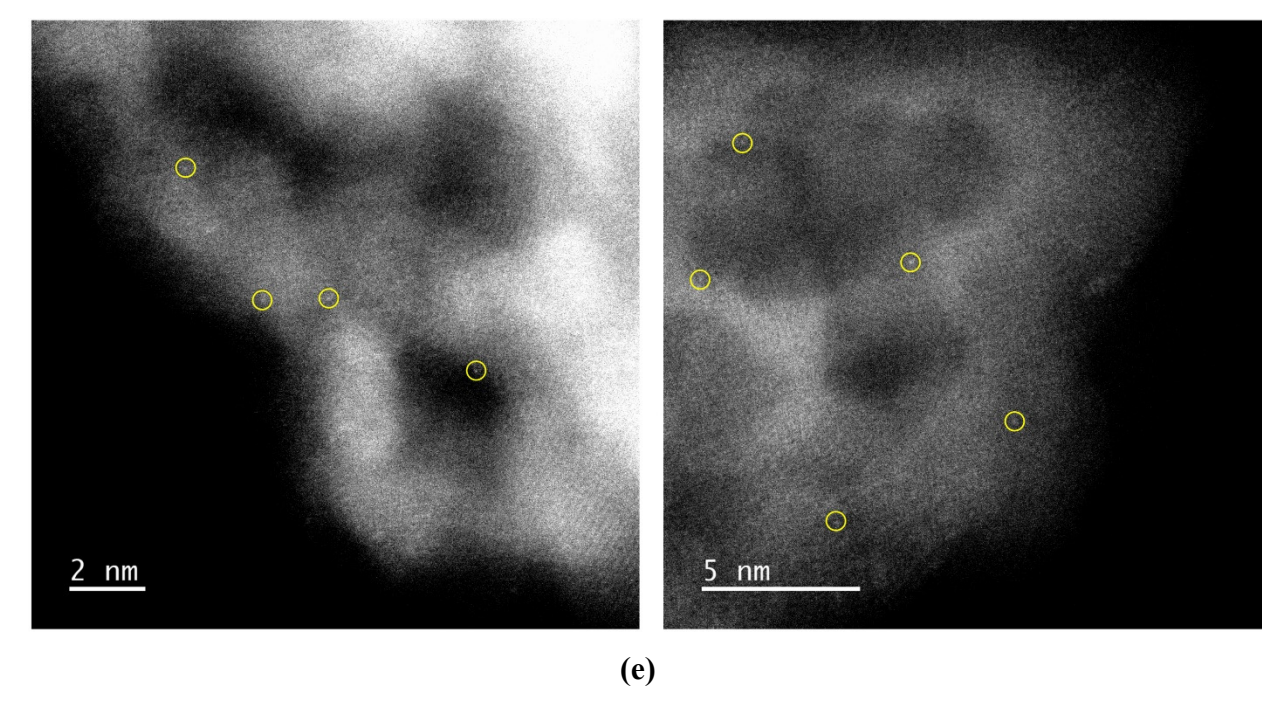


Figure 3. (a) ADF image of the spent 6.4 Fe/Al₂O₃ sample after sulfiding and one cycle of PDH. (b) The EDS map of the region in the box shows Fe and S are well dispersed and no distinct Fe nanophases are visible in the image. (c) ADF image and (d) ABF image of the 6.4 Fe/Al₂O₃ sample after one cycle of PDH. While regions of higher contrast are seen via ADF, they are not associated with any Fe containing crystalline phases. The prominent visible lattice fringes come from alumina, in this case the (400) reflection from gamma alumina 0.198 nm. (e) Higher magnification ADF images of the 6.4 Fe/Al₂O₃ sample after one cycle of PDH. We observe single Fe atoms, as indicated by the yellow circles.

3.3 X-ray Absorption Spectroscopy to determine the structure of the as-synthesized catalyst.

Figure 4a shows the Fe K-edge XANES for the series of Fe/Al₂O₃ catalysts with increasing Fe loading. XANES edge energies and pre-edge peak positions for Fe₂O₃ reference and Fe/Al₂O₃ catalysts are tabulated in **Table S1**. The edge energy and pre-edge peak position did not vary significantly with Fe loading, with the pre-edge peak position being 7113.2 eV and the edge position being 7121.5 eV. This edge position and pre-edge peak were close in value to Fe₂O₃, consistent with the Fe³⁺ oxidation state for all catalysts. The pre-edge peak position of the catalysts is shifted to slightly lower energy and is different in shape compared to the Fe₂O₃ reference, and this is likely due to a difference in point group symmetry of the absorber. Across the loading series,

there were systematic changes in the intensity in the pre-edge region. The pre-edge peak intensity increased with Fe loading, and in the region between the pre-edge peak maximum and the main edge, the intensity systematically increased with Fe loading. This trend has previously been documented in dispersed Fe on Al₂O₃ and was attributed to the formation of extended iron oxide species, and the current results are consistent with this interpretation.³⁰ Based on the surface area of Al₂O₃ used in this study, monolayer coverage of iron is expected to be reached at a Fe loading of 6.4 wt%, however, the intensity increase between 7115-7118 eV appears to increase proportionally with loading rather than abruptly when Fe loading surpasses monolayer coverage. The gradual trend can be rationalized either through the formation of a minority species of crystalline Fe₂O₃ or 2D/oligomeric iron oxide species, both of which would allow for Fe-Fe orbital hybridization responsible for the intensity increase, consistent with STEM results. As the fraction of iron atoms with a nearby iron atom nearby increases, the XANES intensity between 7115-7118 eV increases.

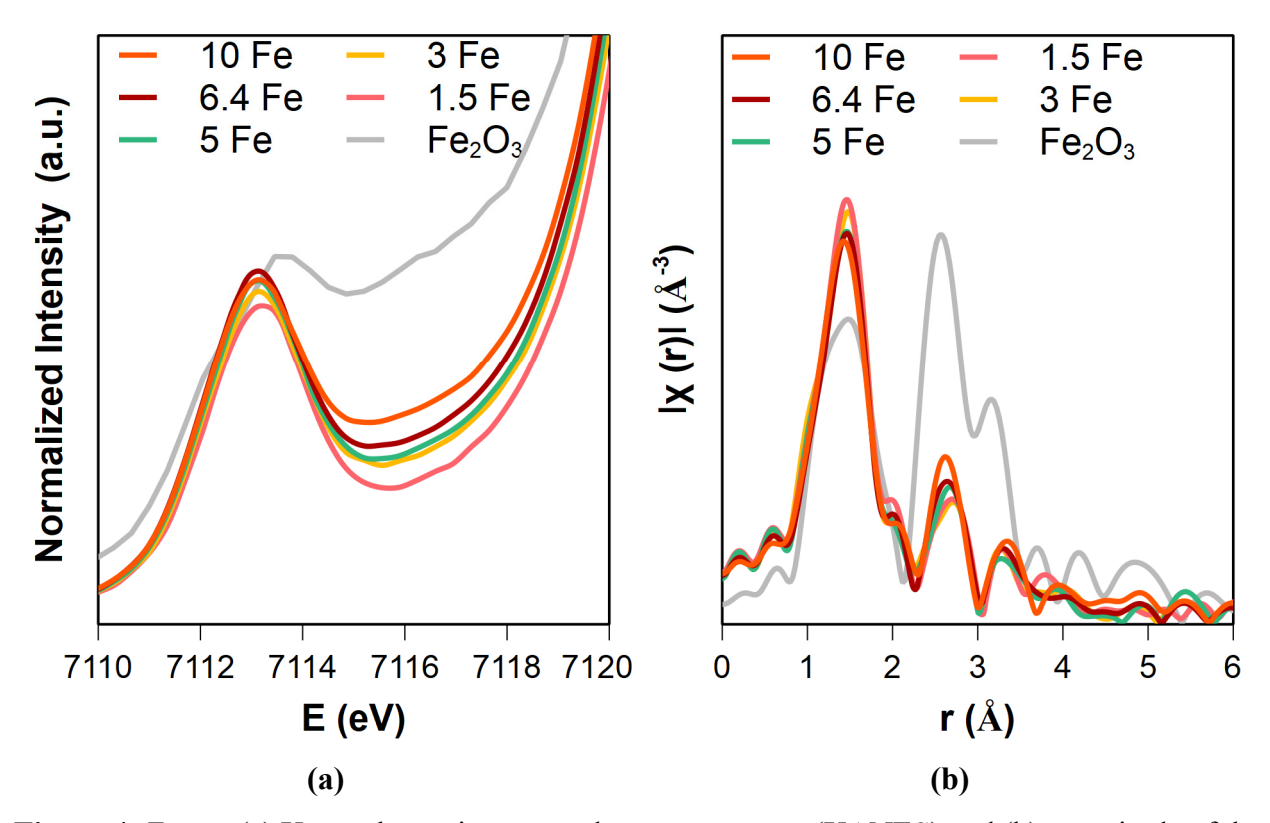


Figure 4. *Ex situ* (a) X-ray absorption near-edge spectroscopy (XANES) and (b) magnitude of the Fourier transform of the EXAFS spectra of as-synthesized 1.5-10 Fe/Al₂O₃ catalysts.

Figure 4b shows the R-space EXAFS spectra Fe/Al₂O₃ catalysts with increasing Fe loading and reference spectra of Fe₂O₃. Fe₂O₃ has three distinct peaks in the local structure seen by EXAFS corresponding to its immediate oxygen environment (1.5Å phase uncorrected distance), and its second and third nearest neighbor iron atoms (2.7, 3.2 Å phase uncorrected distance). In contrast, the Fe-Al₂O₃ catalysts have a more symmetric Fe-O scattering peak and a weak second shell peak. As iron loading increases, the Fe-O scattering peak decreases in intensity, and the second shell peak increases in intensity. Based on the qualitative trends, a model was constructed for the catalysts using the local environment of Fe₂O₃ with Al as the second nearest neighbor. Fitting results are summarized in **Table S2**.

Two models were tested for the first shell Fe-O scattering in 1.5Fe-Al₂O₃, having either one or two Fe-O paths, with results shown in **Figure S12** and **Table S3**. Including a 2nd Fe-O path with a longer bond distance improved the r-factor and reduced chi-squared value of the fit and was then used to model the entire series. Several trends emerged from the fitting results. First, the total Fe-O coordination for the Fe/Al₂O₃ catalysts was about 5, except for 10 Fe/Al₂O₃, which was closer to 6. Unlike Fe₂O₃, the number of short and long Fe-O bonds was not equal, instead of having 4 short bonds (1.92-1.94 Å), and one long bond (2.09-2.11 Å). A previous report on Fe/Al₂O₃ EXAFS similarly modeled one short and one long Fe-O bond distance and obtained similar Fe-O coordination numbers reported here.³⁰ For the short Fe-O bond, the coordination number decreased from 3.9 to 3.3 as Fe loading was increased from 1.5 to 6.4%. The long Fe-O bond also showed small variation between the catalysts (0.9-1.3) though the change was not systematic. The trend in the total Fe-O coordination number could reflect multiple sites of iron adsorption on the Al₂O₃ surface with different oxygen environments that are filled progressively as the Fe loading is increased.

The EXAFS magnitude of the 2nd nearest neighbor of the Fe-Al₂O₃ catalysts is similar in position to that of Fe-Fe scattering in Fe₂O₃ at 2.7 Å (phase uncorrected distance). Examining the imaginary component of the catalyst (**Figure S13** and **Table S4**) and the Q space real component of the peak (**Figure S14**) suggest a lighter scatter such as aluminum. The total Fe-Al coordination number varied between 2-3 among both paths. The lack of Fe-Fe coordination in the second shell of catalysts with Fe loading below 6.4% confirms that most Fe is present as single (or dispersed) sites

in these catalysts. The short Fe-Al path coordination number varied from 0.6-0.9, and the long path varied from 1.2-2.3. This suggests that 2-3 of the oxygen bonds to iron come from bonding with the support, while the remaining (1-2) Fe-O bonds come from an adsorbate or ligand, such as a hydroxyl group or water. EXAFS fittings for Fe foil and Fe/Al₂O₃ catalysts are shown in **Table S5** and **Figures S15** through **S20**.

In line with the monolayer iron coverage predictions, the 10 Fe/Al₂O₃ catalyst could not be modeled using aluminum 2nd nearest neighbors. Instead, a model using Fe-Fe scattering from Fe₂O₃ was used to model the EXAFS. In addition to the Fe-Fe coordination numbers being lower than that of the bulk oxide, the iron environment around the absorber is quite distorted relative to that of bulk Fe₂O₃. In bulk α-Fe₂O₃, Iron has Fe neighbors at 2.899 Å (1 neighbor), 2.968 Å (3 neighbors), and 3.361 Å (3 neighbors). In contrast, 10 Fe/Al₂O₃ was fit with 0.9 neighbors at 3.03 Å, and 2.3 neighbors at 3.56 Å. The lengthening of the Fe-Fe bonds relative to Fe₂O₃ is indicative of lattice expansion. This phenomenon is common in nanoscale oxides, as the diminishing Madelung potential near the oxide surface causes the lattice to expand.⁵⁵ While the Fe-O bond distances are in line with Fe₂O₃, the coordination numbers are not. In bulk Fe₂O₃, Fe has 3 Fe-O bonds at 1.944 Å and 3 bonds at 2.114 Å. In contrast, 10 Fe/Al₂O₃ has 3.9 Fe-O bonds at 1.93 Å, and 1.6 Fe-O bonds at 2.11 Å. As EXAFS is a bulk average technique, these numbers likely reflect a mixture of different Fe-O coordination environments. Given the trend of the XANES, the simplest explanation is that the 10 Fe/Al₂O₃ contains a mixture of Fe single sites, which have a Fe-O coordination number below 6, and small Fe₂O₃ clusters that are 6 coordinate with oxygen. The absence of crystalline α-Fe₂O₃ was ruled out via ex situ Raman measurements shown in Figure S21.

H₂ temperature-programmed reduction (H₂-TPR) experiments. It is known that the reduction behavior of a supported Fe species changes depending on its dispersion, size, and metal-support interaction. $^{56-58}$ Al₂O₃ was utilized as a control and it showed a negligible peak due to its strong metal-oxygen bonds. H₂-TPR profile of bulk iron metal oxide is shown in **Figure 5a**. For Fe₂O₃, at least two distinct peaks were observed at T= 375 °C and 650 °C. For bulk hematite (α-Fe₂O₃), a distinct peak at ~375 °C was assigned to Fe₂O₃ \rightarrow Fe₃O₄ reduction while the broad peak ~650 °C to Fe₃O₄ \rightarrow FeO \rightarrow Fe reduction, similar to the reduction determined by *in situ* XRD. ⁵⁹ For bulk magnetite (Fe₃O₄), one high-temperature broad peak with the highest peak intensity centered

around \sim 760 °C was observed. The reduction of magnetite is expected to follow via Fe₃O₄ \rightarrow FeO \rightarrow Fe.⁵⁹ The multistep reduction generally causes broad reduction envelopes during the second and subsequent reduction step.^{6,60}

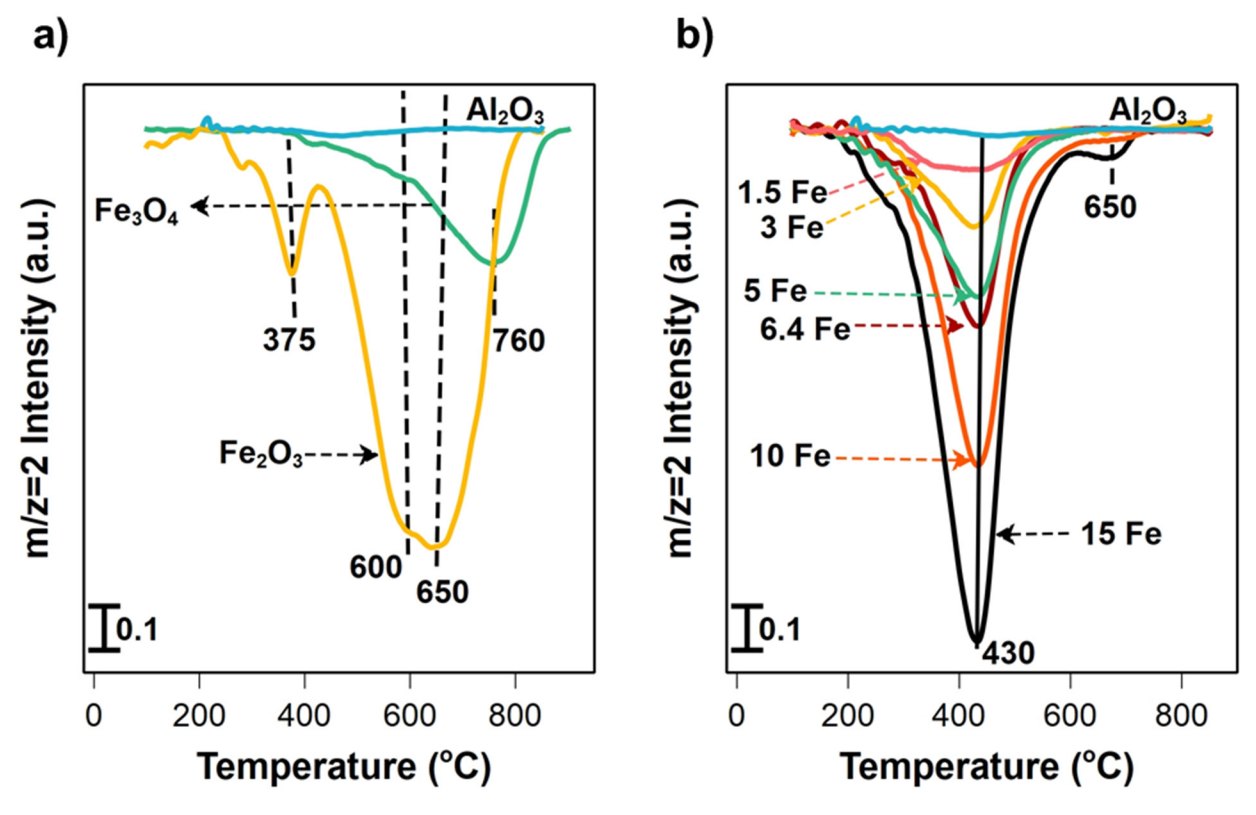


Figure 5. a) Comparison of H₂-TPR profile of bulk iron oxide Fe₂O₃ and Fe₃O₄. b) H₂-TPR profile of as-synthesized Fe/Al₂O₃ catalysts. Fe/Al₂O₃ represents catalyst after calcination in air at 600°C for 4 hr.

To determine the reducibility of the as-synthesized catalysts, H₂-TPR experiments were carried out and the corresponding plots are shown in **Figure 5b**. Only one broad peak with Tp₁ between 350-450°C was observed for Fe/Al₂O₃ catalysts with no broad peak at T > 450 °C, indicating that the catalysts do not possess bulk-like Fe₂O₃ or Fe₃O₄ crystals, consistent with XRD experiments shown in **Figure S2**. The low-temperature peak at ~430 °C can be associated with the reduction of surface Fe³⁺ species. For 15 Fe/Al₂O₃, a satellite peak at 650 °C was observed which may be due to the formation of a minority 3D Fe₂O₃ species due to the higher coverage. ^{30,50,51} This is consistent with XAS results presented in **Section 3.3**, which indicates some agglomeration at higher Fe loading. From **Figure 5b**, it is observed that the peak temperature (Tp) of the supported Fe oxide species appears to be relatively independent of Fe loading over Al₂O₃.

The activated catalysts after H₂S pretreatment (Fe/Al₂O₃-S) were generated and analyzed in situ using H2-TPR. Al₂O₃-S showed a reduction peak at 450 °C, ascribed to loss of surface sulfur species, as shown in Figure 6a.⁴² The reduction peak of bulk FeS, on the other hand, was observed at ~750 °C (Figure 6a inset). 61 In Figure 6a, a single reduction peak was observed during H₂-TPR for all the Fe/Al₂O₃-S catalysts. The peak at ~380 °C for 1.5 to 6.4 Fe/Al₂O₃-S catalysts shifted to a higher temperature for 10 and 15 Fe/Al₂O₃-S at 420 °C. The peak shift to a higher temperature for 10 and 15 Fe/Al₂O₃-S could be due to the formation of an extended structure on the surface of the catalyst. The broad peak at 380-400 °C has previously been attributed to reduction of FeO and Fe₃O₄ to Fe metal. The lack of high-temperature peak evolution (~750 °C) indicates that Fe/Al₂O₃-S catalysts are free of bulk FeS nanoparticles on the surface. The lower H₂ consumption per g of catalyst for H₂S pretreated samples as evinced by H₂-TPR is due to some iron species undergoing easier reduction under H₂S. It was observed that H₂ consumption during H₂-TPR, as observed in Figure 6a, leads to the formation of the H₂S for all catalysts, as shown in Figure 6b. It suggests that the Fe surface species reduction proceeded via Fe-S + $H_2 \rightarrow$ Fe + H_2S , which indicates that the FeS_x species are present on the surface after H₂S pretreatment. These results suggest that after H₂S pretreatment, oxygen neighbor to Fe species is replaced by a sulfur atom.

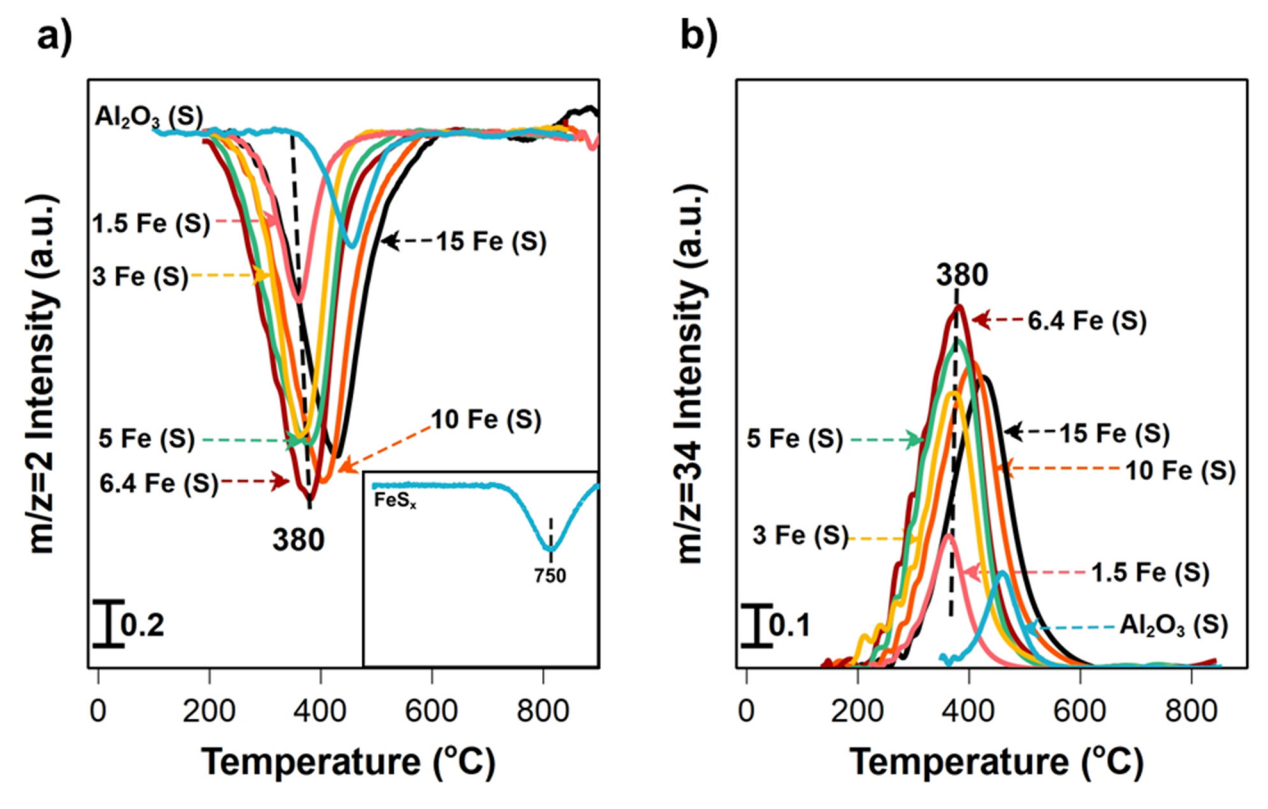


Figure 6. a) H₂ consumption observed during H₂-TPR profile of various Fe loading (wt.%) over Al₂O₃ after H₂S pretreatment. b) H₂S evolution observed during H₂-TPR over various Fe loading (wt.%) over Al₂O₃ after H₂S pretreatment. Fe (S) represents catalyst after H₂S pretreatment at 600 °C for 4 hours. Inset represents H₂-TPR profile for reference FeS sample after H₂S pretreatment at 600 °C for 4 hours.

In **Table 2**, the mmole of H₂ consumed per gram of catalyst is reported. It can be seen that increasing Fe loading up to 6.4 wt.% resulted in an increasing amount of H₂ consumed. Interestingly, it was observed that the amount of H₂ consumed increases on as-synthesized catalyst but remains constant at ca. 0.46 mmole g⁻¹ after 6.4 wt.% Fe loading in H₂S pretreated. It indicates that increasing Fe loading above 6.4 wt.% does not increase the number of reducible FeS_x species. These results are consistent with the presence of a conformal coating of the Fe species on the alumina, over the entire range of loadings. The Fe species remain bound to the alumina and do not form a separate phase. This is why the number of reducible Fe sites do not increase as the loading exceeds the monolayer capacity of alumina for the sulfided Fe species. The monolayer capacity for the sulfided catalyst is reached at the 6.4 Fe catalyst loading.

Table 2. H₂ consumed in mmole per gram of catalyst as obtained from H₂-TPR.

	H ₂ mmole consumed per gram of catalyst		
	(H ₂ consumed per mole of Fe atoms)		
Fe (wt%)	As synthesized	H ₂ S pretreated	
0		0.12	
1.5	0.24 (0.89)	0.23 (0.87)	
3	0.32 (0.59)	0.32 (0.6)	
5	0.45 (0.49)	0.42 (0.46)	
6.4	0.54 (0.47)	0.46 (0.4)	
10	0.77 (0.42)	0.46 (0.26)	
15	1.12 (0.42)	0.44 (0.16)	

3.4 Fixed bed catalytic PDH studies for 10 Fe/Al₂O₃-H₂ and 10 Fe/Al₂O₃-S under different H₂S co-feed conditions.

The catalytic activity for PDH and selectivity towards C₃H₆ with time on stream (TOS) for 10 Fe/Al₂O₃-H₂ and 10 Fe/Al₂O₃-S catalysts in a fixed bed reactor are shown in **Figure 7**. The reaction rate, defined using equation (1), was measured in terms of moles of C₃H₈ consumed per g of catalyst per second. The corresponding propane conversion is reported in **Figure S22**. The 10 Fe/Al₂O₃-H₂ shows an initial activity ~1.1 ×10⁻⁷ moles g⁻¹ s⁻¹, and the initial conversion was 5.6%. An induction period over 10 Fe/Al₂O₃-H₂ was observed, resulting in higher activity (2.69 ×10⁻⁷ moles g⁻¹ s⁻¹, conversion = 13.5% at TOS -10 hours) with TOS. The induction period of about 2 hours before attaining steady-state for 10Fe/Al₂O₃-H₂ could be due to *in situ* formation of the iron carbide phase.⁶ Previously, Tan *et al.*⁶ showed that 10 Fe-P/Al₂O₃ could perform PDH with up to 82% C₃H₆ selectivity at 600 °C. They postulated that the *in situ* Fe₃C phase formation was responsible for high selectivity by comparing pre and post-reaction XRD. Recently, Wang and Senftle, based on electronic structure analyses, suggested that high selectivity of Fe₃C originates from the disruption of surface ensembles via carbon species.⁶²

Previously, Wang *et al.*¹⁸ showed that supported metal oxides (such as Fe, Ni, Co. Mo, Mn, and Cu) upon H₂S pretreatment could perform selective i-C₄ dehydrogenation. Similarly, Sharma *et*

al. 42 showed that H₂S pretreatment and co-feed could dramatically improve the catalytic performance of γ-Al₂O₃. Therefore, the effect of H₂S pretreatment and co-feed was studied over for 10 Fe/Al₂O₃ and shown in **Figure 7** and **Figure S22**. The maximum reaction rate (~1 μmol g⁻¹ s⁻¹) and conversion (43.3%) for 10 Fe/Al₂O₃-S without H₂S co-feed was observed after five minutes of TOS. Afterward, it gradually decreased by ~60% at the end of 10 hr cycle. The effect of different pretreatment conditions can be seen on both selectivity and activity. Notably, the activity is much higher upon H₂S pretreatment. Further, the propylene selectivity for the 10 Fe/Al₂O₃-S (>98%) catalyst was higher than the 10 Fe/Al₂O₃-H₂ (~96%). The increase in rate and selectivity of 10 Fe/Al₂O₃-S could be attributed to *in situ* sulfidation of 10 Fe/Al₂O₃ during H₂S pretreatment, as supported by the temperature program reduction results. The gradual decrease in the observed rate for 10 Fe/Al₂O₃-S was different from 10 Fe/Al₂O₃-H₂. The dramatic drop in activity for 10 Fe/Al₂O₃-S in the absence of H₂S co-feed could be due to loss of sulfur as reported in other work. These catalysts can be regenerated by a combination of H₂S or H₂S/O₂ treatments, as shown in the SI (Figure SXX). We attribute the deactivation to loss of S and possible coke deposition.

Figure 7 also shows the effect of H₂S co-feed on PDH over the 10 Fe/Al₂O₃-S catalyst. The initial selectivity slightly improved from 97.8% in the absence of H₂S to 98.5% in the presence of H₂S co-feed. The deactivation in the presence of H₂S co-feed was also substantially lower. These results indicate that the presence of H₂S is necessary for catalytic stability, and the deactivation could be due to gradual loss of sulfur with time on stream resulting in loss of active sites or formation of an inactive phase. In Importantly, the bulk FeS is not active or possessed a very low rate (selectivity ~65%) compared to the supported Fe/Al₂O₃-S catalysts (**Table S6**). This is in line with Cheng *et al*. Observation where bulk MoS₂ was much less active than supported MoS₂ by a factor of 7 towards i-C₄H₈ dehydrogenation.

Several side reactions can occur at such high operating temperatures, such as coking, thermal cracking to CH₄ and C₂H₄, hydrogenolysis (via *in situ* H₂ produced during dehydrogenation reaction) to crack C₃H₈ to CH₄, C₂H₆. Interestingly, only CH₄ and C₂H₄ were observed as the byproducts, indicating cracking is the primary side reaction in the presence of H₂S co-feed.⁴² The thermal conversion was found low (<0.1%), and the values are provided for reference in **Table S6**.

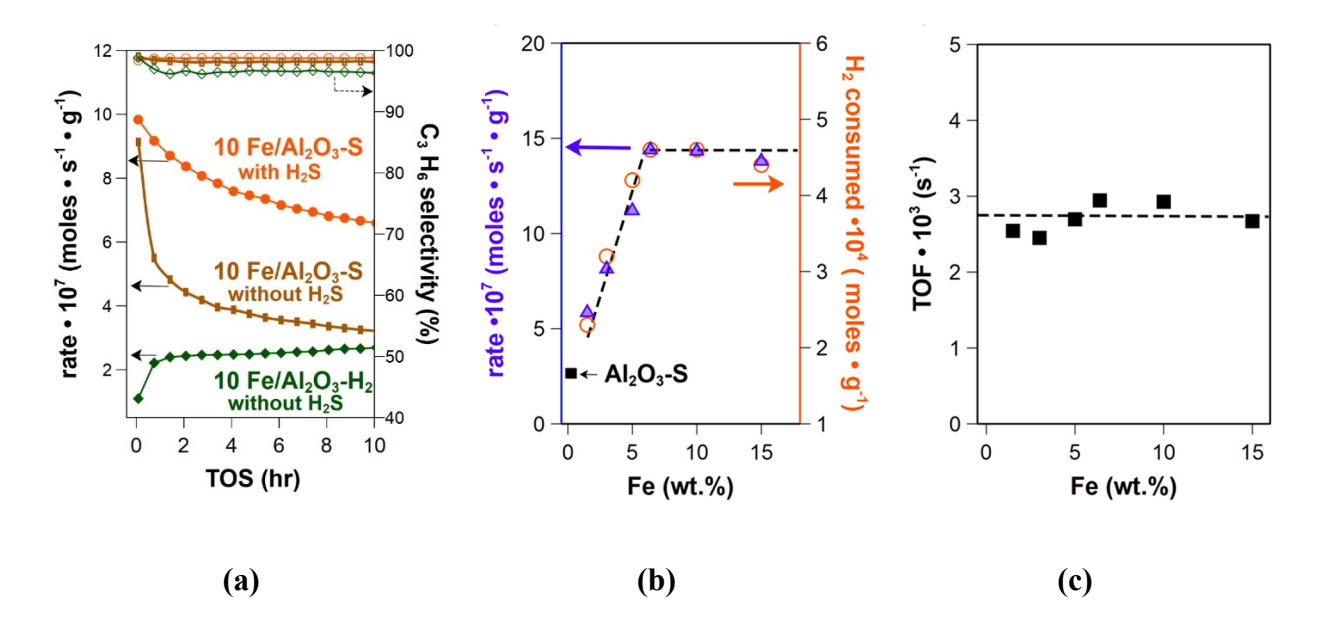


Figure 7. (a) Rate of C₃H₈ consumption and C₃H₆ selectivity for different pretreatments for 10 Fe/Al₂O₃. The feed contained 1.1% C₃H₈, 1% H₂, with (0.1%) and without H₂S co-feed, and the reaction temperature was 560 °C. The 10 Fe/Al₂O₃-H₂ catalyst was pretreated in 1% H₂ at 600 °C for 4 hours. The 10 Fe/Al₂O₃-S catalyst was pretreated in 1% H₂S at 600 °C for 4 hours. The total volumetric flow rate was 50 ml/min and 200 mg of catalyst was used to achieve high conversion (~50%). Solid diamonds, barverts, and octagon represent reaction rate, while empty diamonds, barverts, and octagon represent C₃H₆ selectivity. (b) Rate of C₃H₈ and H₂ consumption as a function of Fe loading wt.% for Fe/Al₂O₃-S catalysts. (c) Turnover frequencies (TOF) for C₃H₈ dehydrogenation as a function of Fe loading wt. %. The feed contained 1.05% C₃H₈, 1% H₂, 0.1% H₂S with the balance N₂, and the reaction temperature was 560 °C. The total volumetric flow rate was 75 ml/min and 30 mg of catalyst was used to achieve differential conversion (<8%). The catalysts were pretreated in a 1 mol% H₂S stream at 600 °C for 4 hrs. The initial rates at TOS = 5mins are reported in the figure. Dashed lines are a guide to the eye.

To study the effect of Fe loading, the reaction conditions such as volumetric flow rate and catalyst mass were optimized to achieve differential conversion <8% (see **Figure S23**) and initial rates are plotted in **Figure 7b**. The high conversion data is also reported in **Table S7**. **Figure 7b** shows the dependence of the rate of C₃H₈ dehydrogenation (at 1.05% C₃H₈, 1% H₂, and 0.1% H₂S at 560 °C) as a function of Fe loading up to 15 wt.%. The C₃H₆ selectivity for Fe/Al₂O₃-S catalysts was about

98.5±0.5, reported in **Table S7**. A linear increase in the rate of C₃H₆ dehydrogenation was observed up to 6.4 wt.% Fe loading, beyond which these rates are essentially independent of the Fe content.

According to previous structural studies, it is reported that the Fe at low loadings leads to highly dispersed iron species. ^{24,31,32} In contrast, at high loadings (above monolayer, i.e., 5 Fe atoms nm²), it can result in hematite-like aggregates. ^{30,50,51} As pointed out using XAS (Section 3.3), that catalyst contains single Fe sites at low loading and can form Fe₂O₃ nanoparticles at higher loading. The plateau in the activity at high loading is indicative of the formation of an inactive phase at high loadings. Importantly, it suggests that the aggregated iron species (such as Fe₂O₃, FeO_xS_y, FeS) are not as active as dispersed Fe sites. Furthermore, the bulk FeS was determined to be inactive toward propane dehydrogenation (see Table S6). Also, a similar selectivity was obtained for all Fe loadings, which indicates that similar sites are responsible for chemistry at all loadings (Table S6 and S7). The H₂ consumption also increased linearly and remains constant at higher loading, i.e., >6.4 wt.% Fe (shown in Table 2) after H₂S pretreatment. The constant rate and H₂ consumption at higher loading reveal increasing iron loading beyond monolayer coverage does not result in the formation of more active sites.

The C₃H₆ dehydrogenation rate normalized per H₂ molecule (TOF) was determined using H₂-TPR is shown in **Figure 7c.** The TOF's invariance with Fe loading suggests that the dehydrogenation of C₃H₈ to C₃H₆ involves only dispersed Fe (FeS_x) site and the rate is dependent on the number of exposed Fe sites. This also indicates that the active sites are reducible by H₂-TPR and H₂ can selectively titrate the active sites. It is generally accepted that propane conversion to propylene can occur over an individual active site of noble metal/metal alloys (such as Pt or Pd) is a structure-insensitive reaction, whereas large ensembles of active sites can also induce structure-sensitive side reactions. ^{1,63–66} It implies that the rate of PDH reaction strongly depends on the number of the active site, and thus, the rate is directly proportional to the number of exposed atoms. Previously, Kim and Wachs studied vanadium oxide catalysts with different VO_x loading for selective methanol oxidation to formaldehyde. ⁶⁷ It was reported in the study that the TOF on these catalysts is independent of the vanadium loading. Similar conclusions were reached for propane ODH over supported vanadium and chromium catalysts. ^{68–70} The constant TOF for propane consumption as a function of surface vanadia coverage indicates that only one surface VO_x site is involved in the

rate-determining step of propane activation. The sum of these previous works suggests that a single surface site can perform selective propane dehydrogenation. In this study, a linear increase in rate up to 6.4 wt.% Fe loading results from the increasing concentration of surface Fe sites. Similar selectivity and TOF at all loadings indicate that a single or dispersed site is required for the chemistry.

The kinetics of propane dehydrogenation was investigated on 6.4 Fe/Al₂O₃-S to determine apparent activation barriers and partial pressure dependence for propane in **Figure 8**. The C₃H₈ conversions of less than 12% are utilized in the temperature range between 540 and 580 °C for plotting the Arrhenius plot. The activation energy value determined was 165 kJ/mol in the temperature range from 540 to 580 °C. The apparent activation energy was similar to obtained for Co and Ru-based catalyst.^{71,72} The reaction order for C₃H₈ was 0.52. The corresponding selectivity, and rate are plotted in **Figure S24** for reference. Next, the effect of H₂S on the reaction kinetics was studied. The reaction order for H₂S was determined to be ~0.20, indicating a promoting effect. The reaction order of ~0.20 for H₂S at either 560 and 600 °C (**Figure S25**) indicates that the effect of H₂S on kinetics is not strongly dependent on the reaction temperature. Of note, high selectivity can be maintained at high temperature and partial pressure of propane, showing that Fe/Al₂O₃-S catalyst potential for industrial applications.

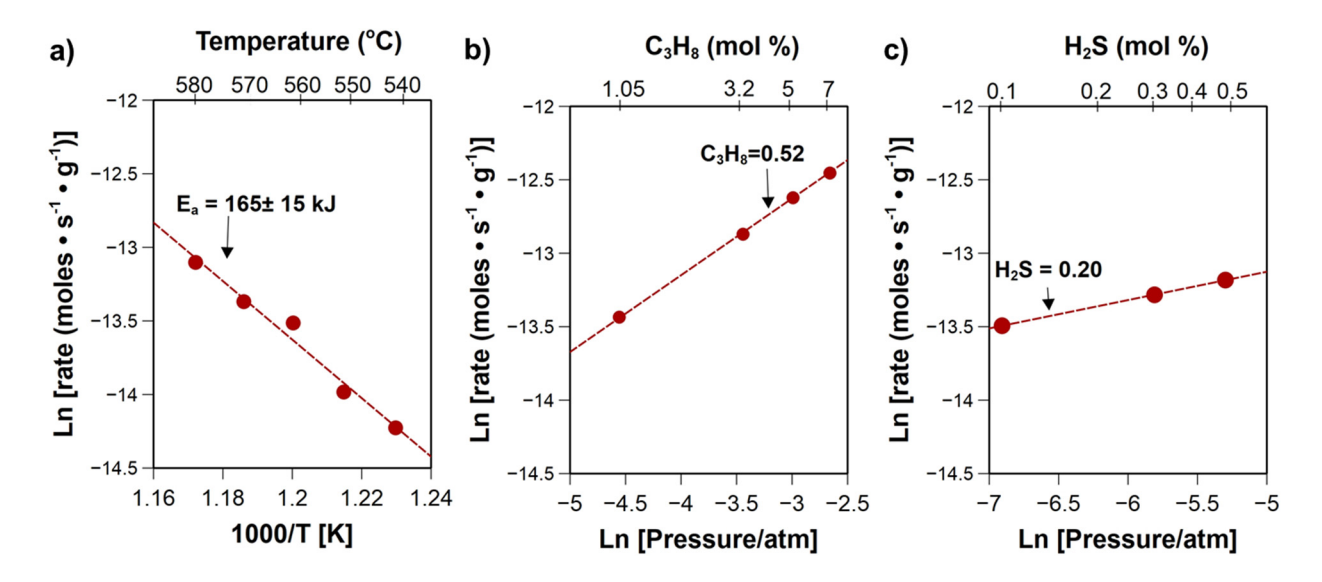


Figure 8. Observed kinetics of propane dehydrogenation reaction on 6.4 Fe/Al₂O₃-S. (a) Arrhenius plot (540–580 °C), with the feed containing 1.05% C₃H₈, 1% H₂, 0.1% H₂S with the balance N₂. Partial pressure dependence of PDH kinetics on (b) propane (varied 1–7 mol %) (c) H₂S (varied

0.1-0.5 mol %) is also shown. The reference concentrations of H₂ and H₂S were 1 and 0.1%, with balance N₂, such that the 30 mg of catalyst and total flow rate of 75 ml/min was ensured; the temperature was fixed at 560 °C to achieve differential conversion (<10%). The catalysts were pretreated in a 1 mol% H₂S stream at 600 °C for 4 hrs. The initial rates at TOS = 5 mins are reported in the figure. The dashed lines are the linear fits to the data.

Finally, summary of the catalytic data available in the literature for mixed or platinum group metalfree catalysts including Sn, Co, Fe, V, Ru for PDH is provided in **Table S8**. While direct comparison is difficult due to the variety of reaction temperatures, feed compositions and H₂S pretreatment (if any), the best catalyst obtained in this work, 6.4 Fe/Al₂O₃-S, exhibited rates an TOF comparable to other non-precious catalysts, chiefly used without H₂S cofeed.

Conclusions

A series of Fe loading (0-15 wt.%) supported over Al₂O₃ catalysts were prepared via the incipient wetness impregnation method. XAS, AC-STEM, BET surface area confirm that the Fe remains atomically dispersed with no bulk nanophases detected. Additionally, EXAFS analysis showed that the second nearest neighbor of iron was aluminum, confirming the single-site nature of iron. Past monolayer coverage, the formation of iron oxide clusters as a minority species was suggested. H₂-TPR was utilized to study the reducibility of the catalyst in as-synthesized and after H₂S pretreatment. In the oxide form, H2-TPR scaled with loading, but H2-TPR results on the sulfided catalyst indicate that the number of exposed Fe sites after H₂S pretreatment increases linearly up to 6.4 wt.% and becomes constant at higher loading for H₂S pretreated samples. This result is explained by the Fe species remaining as a conformal coating on the alumina. Fe/Al₂O₃-S (pretreated with H₂S) showed improved performance compared to Fe/Al₂O₃-H₂; 52% propylene yield along with ~99% C₃H₆ selectivity was obtained over 6.4 Fe/Al₂O₃-S. Like H₂-TPR, the reaction rate as a function of iron loading showed a plateau at higher loading, which corresponds to predicted monolayer coverage of sulfided Fe over Al₂O₃. At loadings above a monolayer, the number of sites do not increase because the Fe remains strongly bound to the alumina, without forming a separate phase. Importantly, it was determined that the TOF was constant irrespective of Fe loading, indicating that propane dehydrogenation rate is constant per Fe site. The constant

TOF values demonstrate that the dispersed Fe site is responsible for the PDH reaction to propylene. The loss of sulfur and some coke deposition was believed to be the main reason for the deactivation of the catalyst since regeneration could be performed utilizing treatment in H₂S with and without oxygen to form the unique and reactive surface sites.

Supporting Information

Catalyst characterization such as TEM, XRD, EXAFS fitting are provided. Additional kinetic data such as conversion, rate, selectivity, and reaction orders at different reaction conditions are tabulated/plotted in the SI.

Acknowledgments

This work is supported by the Center for Understanding and Control of Acid Gas-Induced Evolution of Materials for Energy (UNCAGE-ME), an Energy Frontier Research Center funded by the U.S. Department of Energy, Office of Science, Basic Energy Sciences under grant DE-SC0012577. SR acknowledges support from the American Chemical Society Petroleum Research Fund (Grant# 57946-DNI5). AD acknowledges support from the NSF/ERC CISTAR under Cooperative Agreement EEC-1647722 and microscope acquisition under DMR-1828731. MRCAT operations are supported by the Department of Energy and the MRCAT member institutions. This research used resources of the Advanced Photon Source, a U.S. Department of Energy (DOE) Office of Science User Facility operated for the DOE Offices of Science by Argonne National Laboratory under Contract No. DE-AC02-06CH11357. This research used resources 28-ID-1 of the National Synchrotron Light Source II, a U.S. Department of Energy (DOE) Office of Science User Facility operated for the DOE Office of Science by Brookhaven National Laboratory under Contract No. DE-SC0012704.

Data availability. The data that support the findings of this study are available from the corresponding author upon request.

Lohit Sharma: Investigation (lead); Conceptualization (supporting); Writing – original draft (equal); Writing – review and editing (equal). Stephen Purdy: Investigation (supporting); Writing – original draft (equal); Writing – review and editing (equal). Katharine Page Investigation (supporting); Writing – original draft (equal); Writing – review and editing (equal). Srinivas Rangarajan: Methodology (lead); Supervision (supporting); Conceptualization (supporting); Writing – original draft (equal); writing – review and editing (equal). Hien Pham: Investigation. Abhaya Datye: Investigation; Methodology; Writing – review and editing. Jonas Baltrusaitis: Conceptualization (lead); Methodology (supporting) Funding acquisition; Supervision (lead); Writing – original draft (equal); writing – review and editing (equal).

Competing interests. The authors declare no competing interests.

References

- (1) Sattler, J. J. H. B.; Ruiz-Martinez, J.; Santillan-Jimenez, E.; Weckhuysen, B. M. Catalytic Dehydrogenation of Light Alkanes on Metals and Metal Oxides. *Chem. Rev.* **2014**, *114* (20), 10613–10653. https://doi.org/10.1021/cr5002436.
- (2) Degnan, T. Commercial Catalytic Propane Dehydrogenation (PDH) Technology Offerings Broadened. *Focus Catal.* **2019**, *2019* (11), 1. https://doi.org/https://doi.org/10.1016/j.focat.2019.10.001.
- (3) Jiang, X.; Sharma, L.; Fung, V.; Park, S. J.; Jones, C. W.; Sumpter, B. G.; Baltrusaitis, J.; Wu, Z. Oxidative Dehydrogenation of Propane to Propylene with Soft Oxidants via Heterogeneous Catalysis. ACS Catal. 2021, 11, 2182–2234. https://doi.org/10.1021/acscatal.0c03999.
- (4) Siirola, J. J. The Impact of Shale Gas in the Chemical Industry. *AIChE J.* **2014**, *60* (3), 810–819. https://doi.org/10.1002/aic.14368.
- (5) Otroshchenko, T.; Jiang, G.; Kondratenko, V. A.; Rodemerck, U.; Kondratenko, E. V. Current Status and Perspectives in Oxidative, Non-Oxidative and CO2-Mediated Dehydrogenation of Propane and Isobutane over Metal Oxide Catalysts. *Chem. Soc. Rev.* 2021, 50 (1), 473–527. https://doi.org/10.1039/D0CS01140A.
- (6) Tan, S.; Hu, B.; Kim, W.-G.; Pang, S. H.; Moore, J. S.; Liu, Y.; Dixit, R. S.; Pendergast, J. G.; Sholl, D. S.; Nair, S.; Jones, C. W. Propane Dehydrogenation over Alumina-Supported Iron/Phosphorus Catalysts: Structural Evolution of Iron Species Leading to High Activity and Propylene Selectivity. ACS Catal. 2016, 6 (9), 5673–5683. https://doi.org/10.1021/acscatal.6b01286.
- (7) Schäferhans, J.; Gómez-Quero, S.; Andreeva, D. V; Rothenberg, G. Novel and Effective Copper–Aluminum Propane Dehydrogenation Catalysts. *Chem. A Eur. J.* **2011**, *17* (44), 12254–12256. https://doi.org/10.1002/chem.201102580.
- (8) Hu, B.; Kim, W.-G.; Sulmonetti, T. P.; Sarazen, M. L.; Tan, S.; So, J.; Liu, Y.; Dixit, R. S.; Nair, S.; Jones, C. W. A Mesoporous Cobalt Aluminate Spinel Catalyst for

- Nonoxidative Propane Dehydrogenation. *ChemCatChem* **2017**, *9* (17), 3330–3337. https://doi.org/10.1002/cctc.201700647.
- (9) Mitchell, P. C. H.; Wass, S. A. Propane Dehydrogenation over Molybdenum Hydrotalcite Catalysts. Appl. Catal. A Gen. 2002, 225 (1), 153–165. https://doi.org/https://doi.org/10.1016/S0926-860X(01)00862-6.
- (10) Schweitzer, N. M.; Hu, B.; Das, U.; Kim, H.; Greeley, J.; Curtiss, L. A.; Stair, P. C.; Miller, J. T.; Hock, A. S. Propylene Hydrogenation and Propane Dehydrogenation by a Single-Site Zn2+ on Silica Catalyst. ACS Catal. 2014, 4 (4), 1091–1098. https://doi.org/10.1021/cs401116p.
- (11) Xiong, C.; Chen, S.; Yang, P.; Zha, S.; Zhao, Z.-J.; Gong, J. Structure–Performance Relationships for Propane Dehydrogenation over Aluminum Supported Vanadium Oxide. ACS Catal. 2019, 9 (7), 5816–5827. https://doi.org/10.1021/acscatal.8b04701.
- (12) Szeto, K. C.; Jones, Z. R.; Merle, N.; Rios, C.; Gallo, A.; Le Quemener, F.; Delevoye, L.; Gauvin, R. M.; Scott, S. L.; Taoufik, M. A Strong Support Effect in Selective Propane Dehydrogenation Catalyzed by Ga(i-Bu)3 Grafted onto γ-Alumina and Silica. ACS Catal. 2018, 8 (8), 7566–7577. https://doi.org/10.1021/acscatal.8b00936.
- (13) Wang, H.; Huang, H.; Bashir, K.; Li, C. Isolated Sn on Mesoporous Silica as a Highly Stable and Selective Catalyst for the Propane Dehydrogenation. *Appl. Catal. A Gen.* **2020**, 590, 117291. https://doi.org/https://doi.org/10.1016/j.apcata.2019.117291.
- (14) Han, S.; Zhao, D.; Otroshchenko, T.; Lund, H.; Bentrup, U.; Kondratenko, V. A.; Rockstroh, N.; Bartling, S.; Doronkin, D. E.; Grunwaldt, J.-D.; Rodemerck, U.; Linke, D.; Gao, M.; Jiang, G.; Kondratenko, E. V. Elucidating the Nature of Active Sites and Fundamentals for Their Creation in Zn-Containing ZrO2–Based Catalysts for Nonoxidative Propane Dehydrogenation. ACS Catal. 2020, 10 (15), 8933–8949. https://doi.org/10.1021/acscatal.0c01580.
- (15) Zhang, Y.; Zhao, Y.; Otroshchenko, T.; Lund, H.; Pohl, M.-M.; Rodemerck, U.; Linke, D.; Jiao, H.; Jiang, G.; Kondratenko, E. V. Control of Coordinatively Unsaturated Zr Sites

- in ZrO2 for Efficient C–H Bond Activation. *Nat. Commun.* **2018**, *9* (1), 3794. https://doi.org/10.1038/s41467-018-06174-5.
- (16) Chen, S.; Chang, X.; Sun, G.; Zhang, T.; Xu, Y.; Wang, Y.; Pei, C.; Gong, J. Propane Dehydrogenation: Catalyst Development, New Chemistry, and Emerging Technologies. *Chem. Soc. Rev.* **2021**. https://doi.org/10.1039/D0CS00814A.
- (17) Resasco, D. E.; Marcus, B. K.; Huang, C. S.; Durante, V. A. Isobutane Dehydrogenation over Sulfided Nickel Catalysts. *J. Catal.* **1994**, *146* (1), 40–55. https://doi.org/https://doi.org/10.1016/0021-9517(94)90006-X.
- (18) Wang, G.; Li, C.; Shan, H. Highly Efficient Metal Sulfide Catalysts for Selective Dehydrogenation of Isobutane to Isobutene. *ACS Catal.* **2014**, *4* (4), 1139–1143. https://doi.org/10.1021/cs5000944.
- (19) Wang, G.; Gao, C.; Zhu, X.; Sun, Y.; Li, C.; Shan, H. Isobutane Dehydrogenation over Metal (Fe, Co, and Ni) Oxide and Sulfide Catalysts: Reactivity and Reaction Mechanism. ChemCatChem 2014, 6 (8), 2305–2314. https://doi.org/10.1002/cctc.201402173.
- (20) Cheng, E.; McCullough, L.; Noh, H.; Farha, O.; Hupp, J.; Notestein, J. Isobutane Dehydrogenation over Bulk and Supported Molybdenum Sulfide Catalysts. *Ind. Eng. Chem. Res.* **2020**, *59* (3), 1113–1122. https://doi.org/10.1021/acs.iecr.9b05844.
- (21) Bulánek, R.; Wichterlová, B.; Novoveská, K.; Kreibich, V. Oxidation of Propane with Oxygen and/or Nitrous Oxide over Fe-ZSM-5 with Low Iron Concentrations. *Appl. Catal. A Gen.* **2004**, *264* (1), 13–22. https://doi.org/https://doi.org/10.1016/j.apcata.2003.12.020.
- (22) Kondratenko, E. V; Pérez-Ramírez, J. Oxidative Functionalization of Propane over FeMFI Zeolites: Effect of Reaction Variables and Catalyst Constitution on the Mechanism and Performance. *Appl. Catal. A Gen.* 2004, 267 (1), 181–189. https://doi.org/https://doi.org/10.1016/j.apcata.2004.03.003.
- (23) Sarazen, M. L.; Jones, C. W. MOF-Derived Iron Catalysts for Nonoxidative Propane Dehydrogenation. *J. Phys. Chem. C* **2018**, *122* (50), 28637–28644. https://doi.org/10.1021/acs.jpcc.8b08066.

- Hu, B.; Schweitzer, N. M.; Zhang, G.; Kraft, S. J.; Childers, D. J.; Lanci, M. P.; Miller, J. T.; Hock, A. S. Isolated FeII on Silica As a Selective Propane Dehydrogenation Catalyst. ACS Catal. 2015, 5 (6), 3494–3503. https://doi.org/10.1021/acscatal.5b00248.
- (25) Yun, J. H.; Lobo, R. F. Catalytic Dehydrogenation of Propane over Iron-Silicate Zeolites. *J. Catal.* **2014**, *312*, 263–270. https://doi.org/https://doi.org/10.1016/j.jcat.2014.02.007.
- (26) Sun, Y.; Wu, Y.; Tao, L.; Shan, H.; Wang, G.; Li, C. Effect of Pre-Reduction on the Performance of Fe2O3/Al2O3 Catalysts in Dehydrogenation of Propane. *J. Mol. Catal. A Chem.* **2015**, *397*, 120–126. https://doi.org/https://doi.org/10.1016/j.molcata.2014.11.011.
- (27) Sun, Y.; Wu, Y.; Shan, H.; Wang, G.; Li, C. Studies on the Promoting Effect of Sulfate Species in Catalytic Dehydrogenation of Propane over Fe2O3/Al2O3 Catalysts. *Catal. Sci. Technol.* **2015**, *5* (2), 1290–1298. https://doi.org/10.1039/C4CY01163E.
- (28) Watanabe, R.; Hirata, N.; Miura, K.; Yoda, Y.; Fushimi, Y.; Fukuhara, C. Formation of Active Species for Propane Dehydrogenation with Hydrogen Sulfide Co-Feeding over Transition Metal Catalyst. *Appl. Catal. A Gen.* **2019**, *587*, 117238. https://doi.org/https://doi.org/10.1016/j.apcata.2019.117238.
- (29) Watanabe, R.; Hirata, N.; Fukuhara, C. Active Species of Sulfated Metal Oxide Catalyst for Propane Dehydrogenation. *J. Japan Pet. Inst.* **2017**, *60* (5), 223–231. https://doi.org/10.1627/jpi.60.223.
- (30) Tomita, A.; Miki, T.; Tango, T.; Murakami, T.; Nakagawa, H.; Tai, Y. Fe K-Edge X-Ray Absorption Fine Structure Determination of γ-Al2O3-Supported Iron-Oxide Species. *ChemPhysChem* **2015**, *16* (9), 2015–2020. https://doi.org/10.1002/cphc.201500103.
- (31) Brandenberger, S.; Kröcher, O.; Tissler, A.; Althoff, R. The Determination of the Activities of Different Iron Species in Fe-ZSM-5 for SCR of NO by NH3. *Appl. Catal. B Environ.* **2010**, *95* (3), 348–357. https://doi.org/https://doi.org/10.1016/j.apcatb.2010.01.013.
- (32) Høj, M.; Beier, M. J.; Grunwaldt, J.-D.; Dahl, S. The Role of Monomeric Iron during the Selective Catalytic Reduction of NOx by NH3 over Fe-BEA Zeolite Catalysts. *Appl.*

- Catal. B Environ. **2009**, 93 (1), 166–176. https://doi.org/https://doi.org/10.1016/j.apcatb.2009.09.026.
- (33) Brandenberger, S.; Kröcher, O.; Tissler, A.; Althoff, R. The State of the Art in Selective Catalytic Reduction of NOx by Ammonia Using Metal-Exchanged Zeolite Catalysts. *Catal. Rev.* **2008**, *50* (4), 492–531. https://doi.org/10.1080/01614940802480122.
- (34) Sharma, L.; Brigaityte, O.; Honer, K.; Kalfaoglu, E.; Slinksiene, R.; Streimikis, V.; Sviklas, A. M.; Baltrusaitis, J. Carnallite-Derived Solid Waste as Potassium (K) and Magnesium (Mg) Source in Granulated Compound NPK Fertilizers. *ACS Sustain. Chem. Eng.* **2018**, *6* (7), 9427–9433. https://doi.org/10.1021/acssuschemeng.8b01773.
- (35) Prescher, C.; Prakapenka, V. B. DIOPTAS: A Program for Reduction of Two-Dimensional X-Ray Diffraction Data and Data Exploration. *High Press. Res.* **2015**, *35* (3), 223–230. https://doi.org/10.1080/08957959.2015.1059835.
- (36) Juhás, P.; Davis, T.; Farrow, C. L.; Billinge, S. J. L. PDFgetX3: A Rapid and Highly Automatable Program for Processing Powder Diffraction Data into Total Scattering Pair Distribution Functions. J. Appl. Crystallogr. 2013, 46 (2), 560–566. https://doi.org/10.1107/S0021889813005190.
- (37) Farrow, C. L.; Juhas, P.; Liu, J. W.; Bryndin, D.; Boin, E. S.; Bloch, J.; Proffen, T.; Billinge, S. J. L. PDFfit2 and PDFgui: Computer Programs for Studying Nanostructure in Crystals. *J. Phys. Condens. Matter* **2007**, *19* (33). https://doi.org/10.1088/0953-8984/19/33/335219.
- (38) Kropf, A. J.; Katsoudas, J.; Chattopadhyay, S.; Shibata, T.; Lang, E. A.; Zyryanov, V. N.; Ravel, B.; McIvor, K.; Kemner, K. M.; Scheckel, K. G.; Bare, S. R.; Terry, J.; Kelly, S. D.; Bunker, B. A.; Segre, C. U. The New MRCAT (Sector 10) Bending Magnet Beamline at the Advanced Photon Source. *AIP Conf. Proc.* 2010, 1234 (1), 299–302. https://doi.org/10.1063/1.3463194.
- (39) Kraft, S.; Stümpel, J.; Becker, P.; Kuetgens, U. High Resolution X-Ray Absorption Spectroscopy with Absolute Energy Calibration for the Determination of Absorption Edge

- Energies. Rev. Sci. Instrum. 1996, 67 (3), 681–687. https://doi.org/10.1063/1.1146657.
- (40) Haskel, D. FLUO: Correcting XANES for Self-Absorption in Fluorescence Measurements. University of Washington: Seattle 1999.
- (41) Kiani, D.; Sourav, S.; Wachs, I. E.; Baltrusaitis, J. Synthesis and Molecular Structure of Model Silica-Supported Tungsten Oxide Catalysts for Oxidative Coupling of Methane (OCM). Catal. Sci. Technol. 2020, 10 (10), 3334–3345. https://doi.org/10.1039/D0CY00289E.
- (42) Sharma, L.; Jiang, X.; Wu, Z.; Baltrus, J.; Rangarajan, S.; Baltrusaitis, J. Elucidating the Origin of Selective Dehydrogenation of Propane on γ-Alumina under H2S Treatment and Co-Feed. *J. Catal.* **2021**, *394*, 142–156. https://doi.org/https://doi.org/10.1016/j.jcat.2020.12.018.
- (43) Sharma, L.; Upadhyay, R.; Rangarajan, S.; Baltrusaitis, J. Inhibitor, Co-Catalyst, or Co-Reactant? Probing the Different Roles of H2S during CO2 Hydrogenation on the MoS2 Catalyst. *ACS Catal.* **2019**, *9* (11), 10044–10059. https://doi.org/10.1021/acscatal.9b02986.
- (44) Tischler, L. G.; Angleton; Wing, M. S.; Lake Jackson. Process for Dehydrogenation of Propane. 3,773,850, 1973.
- (45) Xiong, H.; Lin, S.; Goetze, J.; Pletcher, P.; Guo, H.; Kovarik, L.; Artyushkova, K.; Weckhuysen, B. M.; Datye, A. K. Thermally Stable and Regenerable Platinum–Tin Clusters for Propane Dehydrogenation Prepared by Atom Trapping on Ceria. *Angew. Chemie Int. Ed.* **2017**, *129*, 9114–9119. https://doi.org/10.1002/anie.201701115.
- (46) Thommes, M.; Kaneko, K.; Neimark, A. V; Olivier, J. P.; Rodriguez-Reinoso, F.; Rouquerol, J.; Sing, K. S. W. Physisorption of Gases, with Special Reference to the Evaluation of Surface Area and Pore Size Distribution (IUPAC Technical Report). *Pure Appl. Chem.* **2015**, *87* (9–10), 1051–1069. https://doi.org/doi:10.1515/pac-2014-1117.
- (47) Barrett, E. P.; Joyner, L. G.; Halenda, P. P. The Determination of Pore Volume and Area Distributions in Porous Substances. I. Computations from Nitrogen Isotherms. *J. Am*.

- Chem. Soc. 1951, 73 (1), 373–380. https://doi.org/10.1021/ja01145a126.
- (48) Rudolph, M.; Motylenko, M.; Rafaja, D. Structure Model of γ-Al2O3 Based on Planar Defects. *IUCrJ* **2019**, *6*, 116–127. https://doi.org/10.1107/S2052252518015786.
- (49) Yan, W.; Luo, J.; Kouk, Q.-Y.; Zheng, J.; Zhong, Z.; Liu, Y.; Borgna, A. Improving Oxidative Dehydrogenation of 1-Butene to 1,3-Butadiene on Al2O3 by Fe2O3 Using CO2 as Soft Oxidant. *Appl. Catal. A Gen.* **2015**, *508*, 61–67. https://doi.org/https://doi.org/10.1016/j.apcata.2015.10.012.
- (50) Xie, Y.; Xu, X.; Zhao, B.; Tang, Y.; Wu, G. Studies on the Dispersion States of Fe2O3 on γ-Al2O3 by Means of Mössbauer Spectroscopy and XRD. *Catal. Letters* **1992**, *13* (3), 239–245. https://doi.org/10.1007/BF00770996.
- (51) Hoffmann, D. P.; Houalla, M.; Proctor, A.; Fay, M. J.; Hercules, D. M. Quantitative Characterization of Fe/Al2O3 Catalysts. Part I: Oxidic Precursors. *Appl. Spectrosc.* **1992**, 46 (2), 208–218. https://doi.org/10.1366/0003702924125618.
- (52) Botta, P. M.; Aglietti, E. F.; Porto López, J. M. Mechanochemical Synthesis of Hercynite. *Mater. Chem. Phys.* **2002**, 76 (1), 104–109. https://doi.org/https://doi.org/10.1016/S0254-0584(01)00505-3.
- (53) Lee, H.-Y.; Pack, Y.-K.; Lee, B.-K.; Kang, S.-J. L. Discontinuous Dissolution of Iron Aluminate Spinel in the Al2O3–Fe2O3 System. *J. Am. Ceram. Soc.* 1995, 78 (8), 2149–2152. https://doi.org/https://doi.org/10.1111/j.1151-2916.1995.tb08627.x.
- (54) Hoffmann, D. P.; Houalla, M.; Proctor, A.; Hercules, D. M. Quantitative Characterization of Fe/Al2O3 Catalysts. Part II: Reduction, Sulfidation, and CO/Hydrogenation Activity. *Appl. Spectrosc.* **1992**, *46* (3), 489–497.
- (55) Ayyub, P.; Palkar, V. R.; Chattopadhyay, S.; Multani, M. Effect of Crystal Size Reduction on Lattice Symmetry and Cooperative Properties. *Phys. Rev. B* **1995**, *51* (9), 6135–6138. https://doi.org/10.1103/PhysRevB.51.6135.
- (56) Cagnoli, M. V; Marchetti, S. G.; Gallegos, N. G.; Alvarez, A. M.; Mercader, R. C.;

- Yeramian, A. A. Influence of the Support on the Activity and Selectivity of High Dispersion Fe Catalysts in the Fischer-Tropsch Reaction. *J. Catal.* **1990**, *123* (1), 21–30. https://doi.org/https://doi.org/10.1016/0021-9517(90)90154-C.
- (57) Park, J.-Y.; Lee, Y.-J.; Khanna, P. K.; Jun, K.-W.; Bae, J. W.; Kim, Y. H. Alumina-Supported Iron Oxide Nanoparticles as Fischer–Tropsch Catalysts: Effect of Particle Size of Iron Oxide. *J. Mol. Catal. A Chem.* **2010**, *323* (1), 84–90. https://doi.org/https://doi.org/10.1016/j.molcata.2010.03.025.
- (58) Wan, H.; Wu, B.; Xiang, H.; Li, Y. Fischer–Tropsch Synthesis: Influence of Support Incorporation Manner on Metal Dispersion, Metal–Support Interaction, and Activities of Iron Catalysts. *ACS Catal.* **2012**, *2* (9), 1877–1883. https://doi.org/10.1021/cs200584s.
- (59) Jozwiak, W. K.; Kaczmarek, E.; Maniecki, T. P.; Ignaczak, W.; Maniukiewicz, W. Reduction Behavior of Iron Oxides in Hydrogen and Carbon Monoxide Atmospheres. Appl. Catal. A Gen. 2007, 326 (1), 17–27. https://doi.org/https://doi.org/10.1016/j.apcata.2007.03.021.
- (60) Ren-Yuan, T.; Su, Z.; Chengyu, W.; Dongbai, L.; Liwu, L. An in Situ Combined Temperature-Programmed Reduction-Mössbauer Spectroscopy of Alumina-Supported Iron Catalysts. J. Catal. 1987, 106 (2), 440–448. https://doi.org/https://doi.org/10.1016/0021-9517(87)90256-9.
- (61) Li, H.; Liu, J.; Li, J.; Hu, Y.; Wang, W.; Yuan, D.; Wang, Y.; Yang, T.; Li, L.; Sun, H.; Ren, S.; Zhu, X.; Guo, Q.; Wen, X.; Li, Y.; Shen, B. Promotion of the Inactive Iron Sulfide to an Efficient Hydrodesulfurization Catalyst. *ACS Catal.* **2017**, *7* (7), 4805–4816. https://doi.org/10.1021/acscatal.6b03495.
- (62) Wang, P.; Senftle, T. P. Theoretical Insights into Non-Oxidative Propane Dehydrogenation over Fe3C. *Phys. Chem. Chem. Phys.* 2021, 23 (2), 1401–1413. https://doi.org/10.1039/D0CP04669H.
- (63) Childers, D. J.; Schweitzer, N. M.; Shahari, S. M. K.; Rioux, R. M.; Miller, J. T.; Meyer, R. J. Modifying Structure-Sensitive Reactions by Addition of Zn to Pd. *J. Catal.* **2014**,

- *318*, 75–84. https://doi.org/https://doi.org/10.1016/j.jcat.2014.07.016.
- (64) Purdy, S. C.; Seemakurthi, R. R.; Mitchell, G. M.; Davidson, M.; Lauderback, B. A.; Deshpande, S.; Wu, Z.; Wegener, E. C.; Greeley, J.; Miller, J. T. Structural Trends in the Dehydrogenation Selectivity of Palladium Alloys. *Chem. Sci.* 2020, 11 (19), 5066–5081. https://doi.org/10.1039/D0SC00875C.
- (65) Cortright, R. D.; Goddard, S. A.; Rekoske, J. E.; Dumesic, J. A. Kinetic Study of Ethylene Hydrogenation. *J. Catal.* 1991, 127 (1), 342–353. https://doi.org/https://doi.org/10.1016/0021-9517(91)90230-2.
- (66) Chen, S.; Pei, C.; Sun, G.; Zhao, Z.-J.; Gong, J. Nanostructured Catalysts toward Efficient Propane Dehydrogenation. *Accounts Mater. Res.* **2020**, *1* (1), 30–40. https://doi.org/10.1021/accountsmr.0c00012.
- (67) Kim, T.; Wachs, I. E. CH3OH Oxidation over Well-Defined Supported V2O5/Al2O3 Catalysts: Influence of Vanadium Oxide Loading and Surface Vanadium–Oxygen Functionalities. *J. Catal.* 2008, 255 (2), 197–205. https://doi.org/https://doi.org/10.1016/j.jcat.2008.02.007.
- (68) Carrero, C. A.; Schloegl, R.; Wachs, I. E.; Schomaecker, R. Critical Literature Review of the Kinetics for the Oxidative Dehydrogenation of Propane over Well-Defined Supported Vanadium Oxide Catalysts. ACS Catal. 2014, 4 (10), 3357–3380. https://doi.org/10.1021/cs5003417.
- (69) Grant, J. T.; Carrero, C. A.; Love, A. M.; Verel, R.; Hermans, I. Enhanced Two-Dimensional Dispersion of Group V Metal Oxides on Silica. *ACS Catal.* **2015**, *5* (10), 5787–5793. https://doi.org/10.1021/acscatal.5b01679.
- (70) Cherian, M.; Rao, M. S.; Hirt, A. M.; Wachs, I. E.; Deo, G. Oxidative Dehydrogenation of Propane over Supported Chromia Catalysts: Influence of Oxide Supports and Chromia Loading. *J. Catal.* 2002, 211 (2), 482–495. https://doi.org/https://doi.org/10.1006/jcat.2002.3759.
- (71) Dai, Y.; Gu, J.; Tian, S.; Wu, Y.; Chen, J.; Li, F.; Du, Y.; Peng, L.; Ding, W.; Yang, Y. γ-

- Al2O3 Sheet-Stabilized Isolate Co2+ for Catalytic Propane Dehydrogenation. *J. Catal.* **2020**, *381*, 482–492. https://doi.org/https://doi.org/10.1016/j.jcat.2019.11.026.
- (72) Otroshchenko, T.; Kondratenko, V. A.; Rodemerck, U.; Linke, D.; Kondratenko, E. V. ZrO2-Based Unconventional Catalysts for Non-Oxidative Propane Dehydrogenation: Factors Determining Catalytic Activity. *J. Catal.* 2017, 348, 282–290. https://doi.org/https://doi.org/10.1016/j.jcat.2017.02.016.

TOC

